JTTEE5 18:769–793
DOI: 10.1007/s11666-009-9365-7
1059-9630/$19.00 © ASM International

Review of Modeling of Liquid Precursor Droplets and Particles Injected into Plasmas and High-Velocity Oxy-Fuel (HVOF) Flame Jets for Thermal Spray Deposition Applications

Baki M. Cetegen and Saptarshi Basu

(Submitted May 14, 2009; in revised form June 16, 2009)

This article presents a review of the current state-of-the-art in modeling of liquid chemical precursor droplets and particles injected into high-temperature jets in the form of DC-arc plasmas and high-velocity oxy-fuel flames to form coatings. Conventional thermal spray processes have typically utilized powders that are melted and deposited as a coating on hardware surfaces. However, production of coatings utilizing liquid precursors has emerged in the last decade as a viable alternative to powder deposition. Use of liquid precursors has advantages over powder in terms of their relative ease of feeding and tailoring of chemical compositions. In this article, we review the modeling approaches to injection of liquid precursors and particles into plasmas and high-velocity oxy-fuel flames. Modeling approaches for the high-temperature DC-arc plasma and oxy-fuel flame jets are first reviewed. This is followed by the liquid spray and droplet level models of the liquid precursors injected into these high-temperature jets. The various knowledge gaps in detailed modeling are identified and possible research directions are suggested in certain areas.

Keywords HVOF coatings, HVOF process, plasma spray forming, spray deposition, TS coating process

1. Introduction

Production of high-value materials in the form of powders and thin coatings is a large multibillion dollars manufacturing enterprise around the world. Specific functional materials have been synthesized by different processes including spray drying and pyrolysis (Ref 1) as well as combustion and plasma processing (Ref 2). Among the different processing techniques, plasma and high-velocity oxy-fuel (HVOF) flame jet techniques (Ref 2) have been successfully employed for generation of high-value protective coatings on hardware components such as thermal barrier coatings on gas turbine blades and corrosion and wear resistant coatings in other applications. In all these, a powder of the coating material is typically heated in a plasma or HVOF flame jet to deposit partially or fully molten particles onto a substrate forming a thin coating (Ref 2). The velocity and temperatures generated by DC-arc plasma and HVOF flame systems span different ranges and therefore each system is appropriate for different applications. DC-arc systems create plasma jets that have nozzle exit velocities of several hundred meters per second and gas temperatures exceeding 10000 K. On the other hand, HVOF systems produce supersonic gas speeds at the nozzle exit of several kilometers per second and temperatures between 4000 and 6000 K depending on the fuel and oxidizer used.

An alternate route to the typically employed powder injection process into a plasma or HVOF jet is the injection of a liquid spray composed of droplets containing the dissolved salts of the materials to be deposited (Ref 3-6). In this case, droplets injected into a high-temperature plasma or HVOF environment vaporize and concentrate the salt solutes followed by heterogeneous and/or homogeneous nucleation of solid intermediates, their chemical transformations and melting before deposition on a substrate surface. This in situ processing of liquid precursor containing droplets in a high-temperature environment critically determines not only the chemical make-up of the generated coatings but also its microstructural characteristics depending on the thermal, chemical and physical processes that occur at the droplet scale. For example, depending on the heating rate of droplets and the nature of precipitation during heat-up and vaporization phases, different particle morphologies can be obtained including solid particles, hollow shells, and fragmented shells as schematically shown in Fig. 1. When droplets are small and the solute diffusivity is high, increase of solute concentration occurs

Baki M. Cetegen, Mechanical Engineering Department, University of Connecticut, Storrs, CT 06269-3139; and **Saptarshi Basu**, Mechanical, Materials and Aerospace Engineering, University of Central Florida, Orlando, FL 32816. Contact e-mail: cetegen@engr.uconn.edu.

Nomenclature

A_{pore}	total area of the pores
a,b	stoichiometric coefficients in Eq 5
Bi	Biot number
C_D	drag coefficient
$C_{p,d}$	specific heat
d	diameter of the droplets
D_{12}	mass diffusivity of the vapor phase into plasma
D_s	mass diffusivity of zirconium acetate into water
e	internal energy
G_k	turbulence kinetic energy generation due to mean velocity gradient
h	heat transfer coefficient
h_{lv}	latent heat of vaporization for liquid
H	total enthalpy
$\underline{J_i}$	species mass flux vector
$\underline{J_T}$	heat flux vector
k	thermal vector conductivity
Kn	Knudsen number, λ/d
Le	Lewis number, $Le = \alpha/D$
$\dot{m}$	mass flow rate at the droplet surface due to vaporization
P	pressure
Pe	Peclet number
p_v	vapor pressure inside the solid shell
p_∞	pressure outside the droplet
Pr	Prandtl number, $Pr = \nu/\alpha$
$\dot{Q}_c$	conduction heat flux
$\dot{Q}_r$	radiation heat flux
$\dot{Q}_L$	heat transfer rate into the droplet surface
r_s	instantaneous outer radius of the droplet
$\bar{r}_s$	nondimensional radius of the droplet, $\bar{r}_s = r_s/r_0$
R	universal gas constant
Re_d	Reynolds number based on droplet radius and relative velocity between the plasma and droplet
M	Mach number
Nu	Nusselt number
t	time
T	temperature
$\bar{T}$	nondimensional temperature, $\bar{T} = (T - T_0)/T_0$
u	gas or plasma velocity in the x direction
$\underline{u}$	velocity vector
U	axial velocity of the droplet
U_∞	axial plasma velocity
T_d	droplet temperature
r_l	radius of the liquid core
β	non-dimensional surface regression rate = $\beta = \frac{1}{2}\frac{d\bar{r}_s}{d\tau}$
v	gas or plasma velocity in the y direction
V_{pore}	velocity of vapor venting through the pore
$\bar{V}_r, \bar{V}_\theta$	liquid phase velocities within droplet
δ	thickness of the shell
∂	differential operator
$\underline{\nabla}$	gradient operator
χ	mass fraction in the before precipitation regime
χ_s	mass fraction in the liquid core after precipitation regime
$\bar{\chi}$	nondimensional mass fraction, $\bar{\chi} = (\chi - \chi_0)/\chi_0$
η	nondimensional radial coordinate, $\eta = r/r_s$
ν	kinematic viscosity
γ	ratio of specific heats in Eq 13-18
μ	dynamic viscosity
ρ	density
τ	nondimensional time, $\tau = \alpha_L t/r_0^2$
λ	mean free path of gas molecules, α_k
α_k, α_ε	inverse effective Prandtl number for k and ε respectively
ξ	flattening factor
θ	spherical polar angle in droplet coordinates

Subscripts

0	initial value
0	total property in Eq 13-15
l, L	liquid phase
v	vapor phase
∞	far field
p	particle
g	gas phase
s	splat or surface

uniformly throughout the droplet, leading to volumetric precipitation and consequently forming solid particles as shown as path (A) in Fig. 1. When rapid vaporization occurs on the droplet surface and the solute diffusivity is low such that a high solute concentration builds up around the droplet periphery, as shown in path B in Fig. 1, there could be different outcomes including fragmented shells (B-I) as a result of internal pressurization for low vapor permeability through the formed shell, hollow spherical shells (B-II) for the case of high permeability through the shell, or rapid disintegration of the shell containing some of the liquid leading to secondary atomization (B-III) as a result of rapid internal pressurization and shell rupture. Another path is that of formation of a plastic shell that inflates due to internal liquid vaporization and eventual rupture and collapse of the deformed shell (path C in Fig. 1). The morphology of the formed deposits and coating microstructure is naturally affected by the produced particle morphologies and their impact conditions that form the coating. In this review article, we first survey the modeling studies on DC-arc plasmas and HVOF jets. This is followed by presentation of particle and droplet level models, precursor chemistries and precipitation kinetics as well as some results from previous modeling studies.

2. Thermo-Fluid Modeling of DC-Arc Plasmas

DC-arc plasmas employed in thermal spray applications (Ref 2) utilize a continuous arc break-down in a gas mixture flowing between the anode and cathode of a

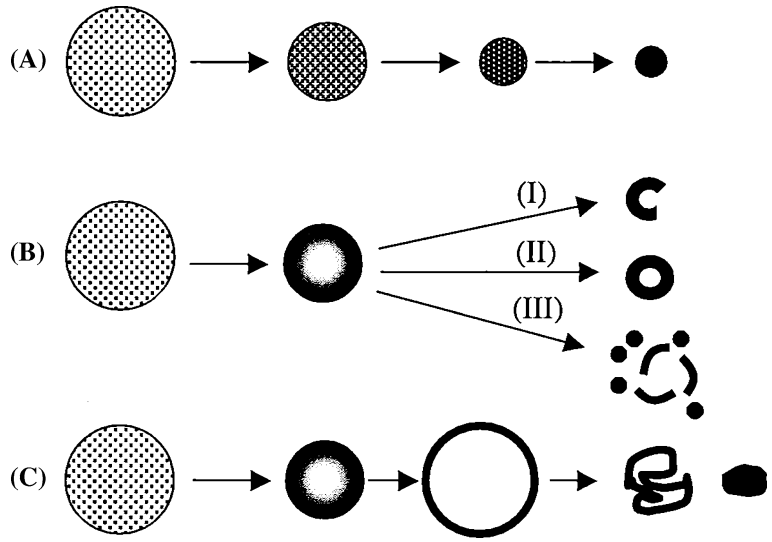

Fig. 1 Solute containing droplet vaporization and precipitation routes: (A) uniform concentration of solute and volume precipitation leading to solid particles; (B) supersaturation near the surface followed by (I) fragmented shell formation (low permeability through the shell, (II) unfragmented shell formation (high permeability), (III) impermeable shell formation, internal heating, pressurization and subsequent shell break-up and secondary atomization from the internal liquid; (C) elastic shell formation, inflation and deflation by solids consolidation

plasma generator as schematically shown in Fig. 2. Ionized gases from the feed gas stream (Ar, He, N_2, H_2 mixtures) emerge from a plasma nozzle assembly at high velocities of the order of several hundred meters per second and temperatures exceeding 10000 K (Ref 7). Modeling of these high-temperature gases containing ionized and neutral species and electrons constitutes a very challenging task. Literature contains significant amount of work on thermo-fluid modeling of DC-arc plasmas (Ref 8-25). The detailed simulations include numerical solution of the chemically reacting flow (Navier-Stokes) equations including the charged species. These equations include conservation of mass, momentum and species with specified chemical source terms and closure equations. Turbulence is accounted for by k-ε or other subgrid models. The governing equations take the following forms:

$$\text{Continuity:}\quad \frac{\partial(x^n\rho)}{\partial t}+\underline{\nabla}\cdot(x^n\rho\underline{u})=0 \qquad \text{(Eq 1)}$$

$$\text{Species:}\quad \frac{\partial(x^n\rho_i)}{\partial t}+\underline{\nabla}\cdot(x^n\rho_i\underline{u})=-\underline{\nabla}\cdot(x^n\underline{J}_i)+x^n\dot{\rho}_i^c \qquad \text{(Eq 2)}$$

$$\text{Momentum:}\quad \frac{\partial(x^n\rho\underline{u})}{\partial t}+\underline{\nabla}\cdot(x^n\rho\underline{u}\underline{u})=-\underline{\nabla}\left(p+\frac{2}{3}\rho k\right)+\underline{\nabla}\cdot\sigma \qquad \text{(Eq 3)}$$

$$\text{Energy:}\quad \frac{\partial(x^n\rho\underline{e})}{\partial t}+\underline{\nabla}\cdot(x^n\rho\underline{u}e)=-p\underline{\nabla}(x^n\underline{u})-\underline{\nabla}\cdot(x^n\underline{J}_T)+x^n(\Phi+\dot{Q}_c-\dot{Q}_r) \qquad \text{(Eq 4)}$$

In these equations, $n=0$ for two and three dimensions in Cartesian coordinates and $n=1$ for two-dimensional axisymmetric configuration with x representing the radial coordinate. The symbols used in these equations are defined in the nomenclature. These equations are supplemented by the reaction rates of the type,

$$\sum_r a_r R_r \leftrightarrow \sum_p b_p P_p \qquad \text{(Eq 5)}$$

with each reaction having a specified reaction rate that determines the species production/depletion rates $\dot{\rho}_i^c$. Typically the kinetic reaction rates are specified in Arrhenius form and fast reactions are considered to be in equilibrium while the slower reactions proceed at their kinetic rates. The system of equations is closed by specifying the diffusion fluxes for mass (J_i) and heat (J_T). Radiative losses are modeled as a temperature dependent energy sink. Solution of the system of equations has been implemented in computational codes such as LAVA (Ref 8, 9). Figure 3 shows some results from Ramshaw and Chang (Ref 8) on the radial and axial distributions of plasma temperature for an axisymmetric Argon plasma issuing into a room temperature Argon medium. In this study, the computed temperature profiles were found to be in reasonable agreement with the experiments performed by Dilawari et al. (Ref 10) at Idaho National laboratories. One of the issues in comparisons of model predictions with experiments is the application of the appropriate boundary conditions in the model. Often, experiments do not provide sufficiently detailed inlet measurements of velocities, temperatures, densities and species distributions (neutrals, ions and electrons) to provide well-defined inlet conditions for the model. This is

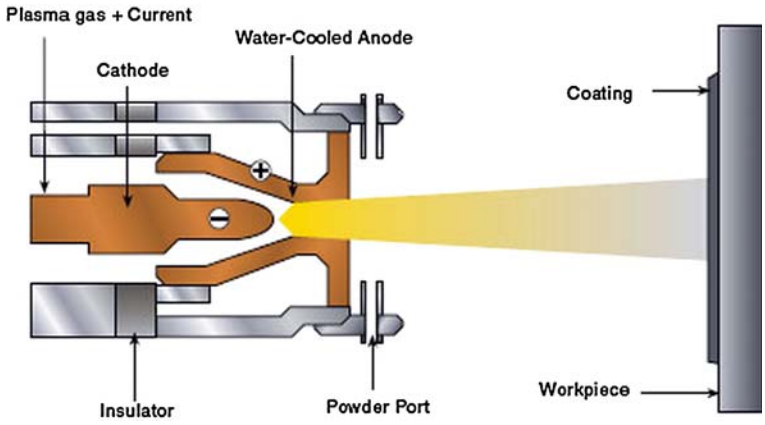

Fig. 2 Internal geometry of a DC-arc plasma torch (from Sulzer Metco)

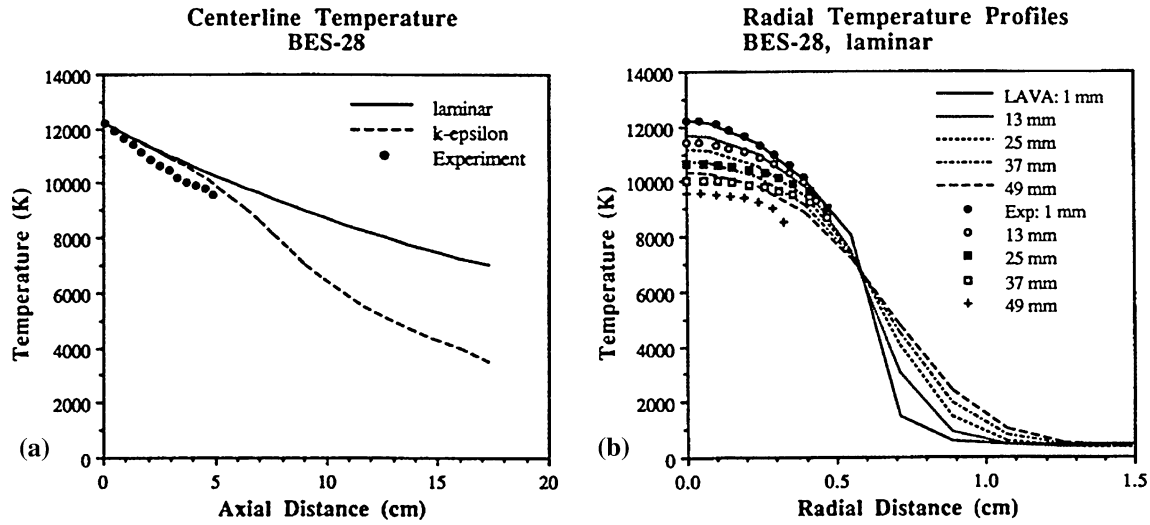

Fig. 3 Computed and measured plasma temperature profiles from Ref 8: (a) axial profile; (b) radial profile

not due to the lack of interest in measuring these parameters, but the difficulty or inability of obtaining such data from experiments. One of the assumptions in many of the plasma simulations is the existence of local thermodynamic equilibrium (LTE) which simplifies the plasma thermal field description. In atmospheric pressure DC-arc plasmas that are typically employed in thermal spray applications, the justification for LTE has been made (Ref 7). However, nonequilibrium effects have been also studied by Chang and Ramshaw (Ref 9) which show that LTE approximation can break down under certain conditions and in some regions of a plasma jet.

Another issue with DC-arc plasma simulations is the arc root fluctuations creating unsteadiness at the plasma jet origin. These fluctuations with frequencies in the range of several kilohertz have been experimentally observed and modeled (Ref 11-13), an example of which is shown in Fig. 4 from Ref 13. Complex inner geometry of DC-arc plasma chambers and the presence of an electrical arc within this chamber necessitate the injection of thermal spray materials (powders or sprays) external to the plasma chamber. Typically, a droplet or particle laden jet of some carrier gas is directed normal to the plasma jet axis in order for the material to be entrained into the high-temperature plasma. This injection scheme naturally distorts the axisymmetry of the plasma jet and induces three-dimensional effects. Li and Chen (Ref 16) modeled the three-dimensional field of an Argon plasma jet and showed that the carrier gas jet results in displacement of the plasma jet centerline from the axis with increasing carrier jet velocity. Although the plasma temperature distributions do not seem to be greatly affected, the calculated particle temperature histories and their distributions show significant variations. The radial location of the injector with respect to the plasma jet orifice has been shown to be a critical parameter in addition to the carrier gas to plasma stream momentum ratio.

Simultaneous solution of the plasma flow field in the presence of droplets is not feasible and typically plasma flow field is first computed and the particle/droplet

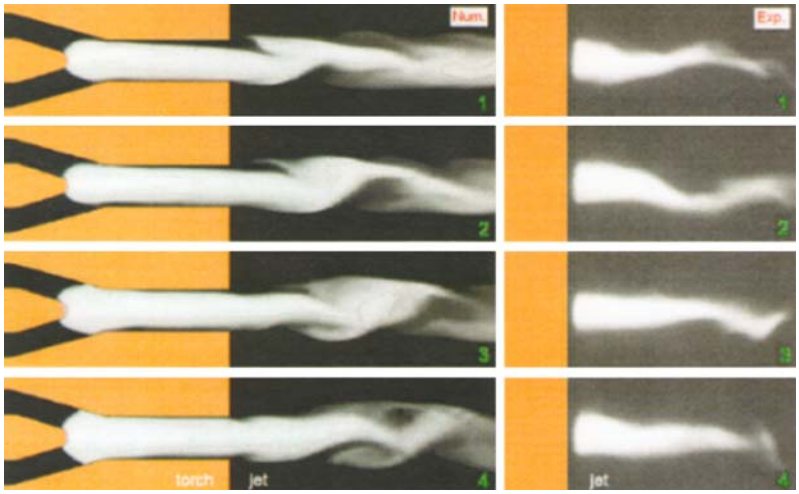

Fig. 4 Arc and plasma jet dynamics: sequence of instantaneous heavy particle temperature distribution obtained numerically (num) and experimentally (exp). Time intervals between frames is 100 μs for numerical results and 2 ms in the experiments from Ref 13

interaction is considered as a separate discrete phase Lagrangian model utilizing the plasma temperatures, velocities and plasma properties. This approach usually neglects the two-way coupling between the plasma gas and the droplet liquid phases (i.e. influence of the discrete phase on the plasma gas field) and only considers the influence of the plasma flow field on the injected particles/droplets. Literature contains a number of studies that deal with the prediction of particle temperatures in plasmas (Ref 15-25). In many of these studies, the particle heat transfer is formulated in terms of heat conduction potential and a temperature slip between particle and plasma gas. For small particles, the Knudsen number $Kn = \lambda/d$, where λ is the mean free path distance for gas molecules and d is the particle diameter, could be large enough for the continuum approximation for heat transfer not to hold true (i.e. $Kn \geq 1$). In these situations, particle heat transfer calculations have to incorporate the slip flow and free molecular flow regimes as appropriate. All computations deal with spherical particle heat up, melting and eventual vaporization and particles injected into the plasma take different paths and consequently follow different temperature histories (Ref 23, 24). Depending on the material particles are composed of and the convective heat transfer conditions, the Biot number $Bi = hd/k_p$, where h is the convective heat transfer coefficient, d is the particle diameter and k_p is the particle thermal conductivity, determines the importance of the temperature gradients internal to the particle. In cases where Bi is small, the particle internal temperature gradients are small and lumped capacity heat transfer analysis becomes appropriate. When $Bi > 0.1$, the particle internal temperature field needs to be considered as a part of the computations. Effects of particle-particle interactions have also been considered and quantified. A general modeling approach that has been used in the field is schematically shown in Fig. 5. It includes the modeling of gas dynamics of the thermal spray torch followed by predictions of droplet breakup, droplet or particle transport (momentum, mass, heat) processes and finally models of particle deposition and coating formation.

3. Thermo-Fluid Modeling of High-Temperature Oxy-Fuel Flame Jets

HVOF flame process has been used as a primary method for generating metallic and in some cases ceramic coatings in industrial applications. It has evolved as an improved method to modify surface properties enhancing the product life, durability, thermal resistance and corrosion resistance. Different industries such as aerospace, power generation and automotive are heavily dependent on HVOF thermal spray processes to generate functional coatings. Coatings produced by oxy-fuel spraying are typically dense coatings. HVOF process is normally used for generating coatings with lower melting temperature, like WC-Co, Cr_3C_2-NiCr etc. (Ref 26). Wear resistant coatings using tungsten carbide, cobalt or nickel based materials are some common applications of HVOF process (Ref 27, 28). Because of its relatively low temperature, HVOF process is rarely used for ceramic coating application (Ref 26). There are however some exceptions where certain types of HVOF systems such as HV2000 have been used for thermal barrier coating application.

Different designs of the HVOF torches have been used in industry, although the core technology is similar in all cases. Figure 6 (Ref 29) shows a schematic of a HVOF torch. It consists of a unit that incorporates a combustion chamber and a converging-diverging nozzle for accelerating the combustion products to supersonic speeds. The combustion process takes place inside the torch. The torch houses three annular ports for injecting powder, fuel-oxygen mixture and air. Coating materials are injected in the form of powder with a carrier gas (generally N_2) through an axial inlet port. A water cooled jacket surrounds the nozzle to protect the torch from overheating.

Premixed fuel and oxygen are supplied into the HVOF combustion chamber. In industry different types of HVOF torches are used. Few of the commonly used torches are HV2000, JP-5000 by Praxair and Diamond Jet hybrid torch by Sulzer Metco. There are also different types of fuels used for the HVOF process. Among gaseous fuels, propylene (C_3H_6) is the most common variety while kerosene is preferred by many industries as an alternative liquid fuel. Hydrogen has also been used in cases where high temperatures and carbon free deposits are desired.

Depending on the applications, materials are injected either in the form of liquid precursors or in the form of solid particles. For ceramic coatings, generally solution precursor is preferred. In this case, liquid precursors are injected as a spray of small droplets into the high-velocity combustion gases. The droplet injectors are usually placed outside the torch or very close to nozzle exit. In some cases, liquid may be injected as a stream which undergoes breakup into droplets in the high shear turbulent flow field of the HVOF jet. For metallic coatings, normally powder injection is preferred. Powders containing micron-size metal or metal-alloy particles are injected into the torch. The quality and density of produced coatings depend on temperatures and velocities that particles or droplets attain before impacting on a substrate. It is important to note that the particle/droplet temperature and velocity are dependent on fuel-oxygen ratio, mass flow rates of gases as well as the powder/precursor type, injection location, spray distance, size and residence time of the particles or droplets. As shown in Fig. 7 (Ref 29), there are multitude of processes that ultimately affect the coating quality including the dynamics of the HVOF jet. We will first discuss the modeling of gas dynamics in an HVOF torch. The modeling of the HVOF gas dynamics includes heat, mass and momentum transport and combustion processes. The pre-mixed fuel and oxygen are injected into the combustion chamber. The HVOF process is a multi-phase process which involves discrete phase (particles or droplets) interacting with the continuum gas phase. Though gas dynamics and the particle dynamics influence each other, the particle effects on the gas phase are typically neglected. Particle loadings less than 4% by volume have been determined not to substantially affect the gas dynamics. Thus, the modeling typically considers only one-way coupling of the gas flow affecting the particles.

The modeling of combustion process within the torch can be dealt with at different levels. The simplest model assumes that the combustion of the fuel and oxidizer is complete and reaches chemical equilibrium. A more detailed approach includes the overall chemical reaction rate between fuel and oxidizer and the corresponding heat release rate. A more comprehensive approach involves more detailed modeling of combustion process by a reduced chemical kinetic mechanism. In thermal spray process modeling, a computational approach that captures the gas composition, thermal and flow fields in a sufficiently accurate manner is adequate as computation of detailed gas species distributions may not add much to the accuracy of the particle heat-up results.

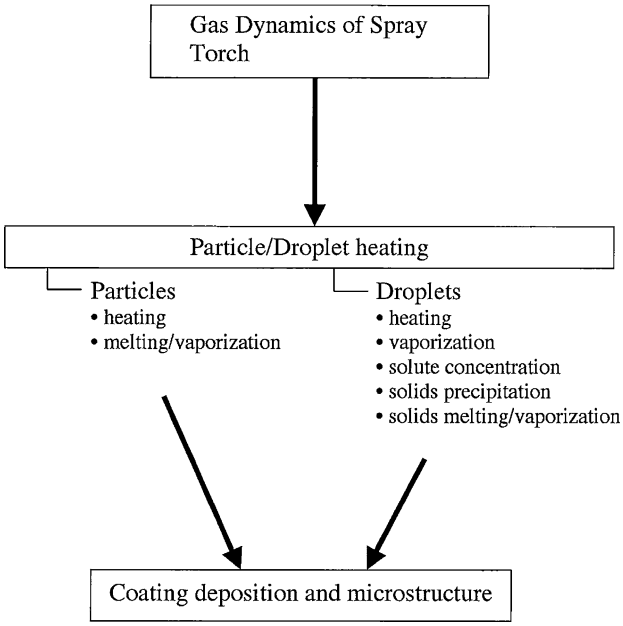

Fig. 5 Modeling steps for thermal spray process utilizing solid or liquid feedstock

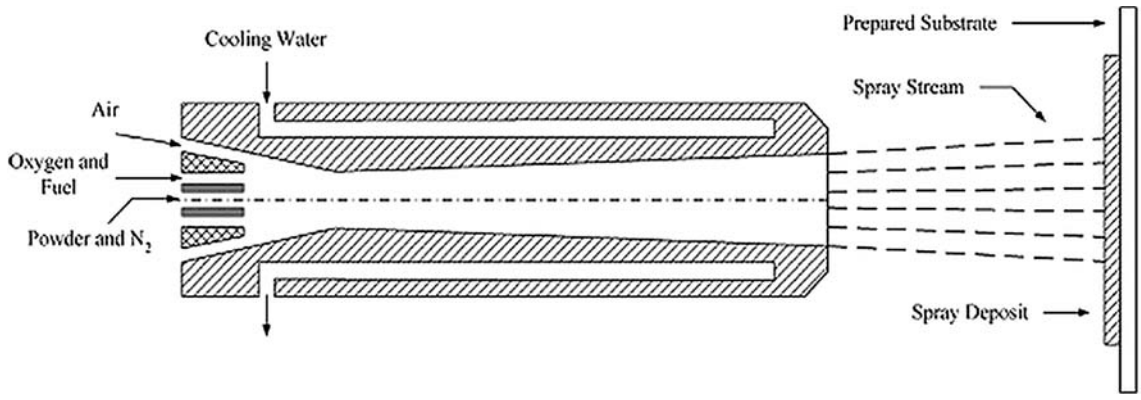

Fig. 6 Schematic of diamond jet hybrid HVOF process (Ref 29)

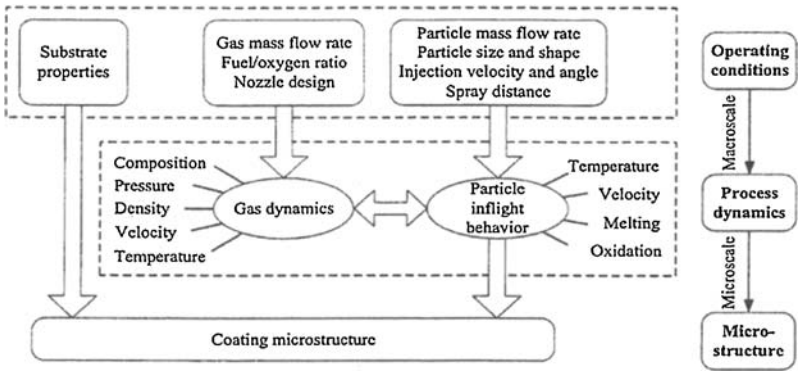

Fig. 7 Processes in an HVOF torch (Ref 29)

The governing equations for gas phase modeling include mass, momentum [Compressible Navier Stokes] and energy conservation. However, the highly turbulent nature of the flow and consequently its high Reynolds number make direct numerical simulation intractable. Therefore, turbulence closure models along with Reynolds or Favre averaged governing equations are employed to obtain time averaged results and relevant flow statistics. The Reynolds averaging for any variable (like velocity, temperature) is formulated as (Ref 30), $\phi = \bar{\phi} + \phi'$, with $\bar{\phi} = \frac{1}{\Delta t}\int_{t_0}^{t_0+\Delta t} \phi\, dt$ and $\bar{\phi}' = 0$. On the other hand, Favre average is formulated in a slightly different way as, $\phi = \tilde{\phi} + \phi''$, with $\tilde{\phi} = \frac{\overline{\rho\phi}}{\bar{\rho}}$ and $\tilde{\phi}'' = 0$. After incorporating the time averaged quantities, the governing equations reduce to (Ref 30),

Continuity

$$\frac{\partial \bar{\rho}}{\partial t} + \frac{\partial}{\partial x_i}(\bar{\rho}\tilde{v}_i) = 0 \qquad \text{(Eq 6)}$$

and momentum equation:

$$\frac{\partial(\bar{\rho}\tilde{v}_j)}{\partial t} + \frac{\partial}{\partial x_i}(\bar{\rho}\tilde{v}_j\tilde{v}_i) = -\frac{\partial \bar{\rho}}{\partial x_j} + \frac{\partial}{\partial x_i}\left[\mu\left(\frac{\partial \tilde{v}_j}{\partial x_i} + \frac{\partial \tilde{v}_i}{\partial x_j} - \frac{2}{3}\delta_{ji}\frac{\partial \tilde{v}_l}{\partial x_l}\right)\right] + \frac{\partial}{\partial x_i}\left(-\bar{\rho}\overline{v_i'' v_j''}\right) \quad j = 1,2,3 \qquad \text{(Eq 7)}$$

where P, ρ and μ are pressure, density and molecular viscosity of the gases. x_i is the coordinate and the term $-\bar{\rho}\overline{v_i'' v_j''}$ is the Reynolds stress term indicating the effect of turbulence. Closure of the Reynolds stress terms is taken into account by considering RNG k-ε model. These equations are generally of the form (Ref 30)

$$\frac{\partial(\bar{\rho}k)}{\partial t} + \frac{\partial}{\partial x_i}(\bar{\rho}\tilde{v}_i k) = \frac{\partial}{\partial x_i}\left[\alpha_k(\mu + \mu_t)\frac{\partial k}{\partial x_i}\right] + G_k - \bar{\rho}\varepsilon - Y_M \qquad \text{(Eq 8)}$$

and

$$\frac{\partial(\bar{\rho}\varepsilon)}{\partial t} + \frac{\partial}{\partial x_i}(\bar{\rho}\tilde{v}_i\varepsilon) = \frac{\partial}{\partial x_i}\left[\alpha_\varepsilon(\mu + \mu_t)\frac{\partial \varepsilon}{\partial x_i}\right] + C_{1\varepsilon}\frac{\varepsilon}{k}G_k - C_{2\varepsilon}\bar{\rho}\frac{\varepsilon^2}{k} - R_\varepsilon \qquad \text{(Eq 9)}$$

where ε represents the turbulence dissipation, G_k designates the generation of turbulence kinetic energy due to mean velocity gradient, Y_M models the effect of fluctuation dilatation to global dissipation, R_ε is the additional term in Eq 9 responsible for accuracy of the model in highly strained flow field. α_k and α_ε are inverse effective Prandtl number for k and ε, respectively.

For reacting flows as in HVOF, mass conservation of the each species can be written as (Ref 30),

$$\frac{\partial(\bar{\rho}Y_j)}{\partial t} + \frac{\partial}{\partial x_i}(\bar{\rho}Y_j\tilde{v}_i) = -\frac{\partial}{\partial x_i}[J_j] + R_j \qquad j = 1,2,3\ldots N-1 \qquad \text{(Eq 10)}$$

J_i is the diffusion flux of ith species calculated by Maxwell-Stefan equation and N is total number of species involved in the process. R_j is the rate of production of species "j". The energy equation can be formulated as (Ref 30),

$$\frac{\partial(\bar{\rho}H)}{\partial t} + \frac{\partial}{\partial x_j}[\tilde{v}_j(\bar{\rho}H + \bar{p})] = \frac{\partial}{\partial x_i}\left[\alpha c_p(\mu + \mu_t)\frac{\partial T}{\partial x_i} + \tilde{v}_j(\mu + \mu_t)\left(\frac{\partial \tilde{v}_i}{\partial x_j} + \frac{\partial \tilde{v}_j}{\partial x_i} - \frac{2}{3}\delta_{ji}\frac{\partial \tilde{v}_l}{\partial x_l}\right) - \sum_{j=1}^{N} J_j H_j\right] + S_E \qquad \text{(Eq 11)}$$

where T is the temperature and H is total enthalpy, S_E stands for source terms like heat generation. The total enthalpy can be defined as (Ref 30)

$$H = \sum_j Y_j H_j. \qquad \text{(Eq 12)}$$

The computational time increases significantly with increase in number of species. Many studies hence have implemented the eddy dissipation model to simplify the problem. Eddy dissipation model assumes infinitely fast reaction process and the reaction rate is limited by turbulent mixing rate of fuel and oxidants. With the eddy dissipation model, proper analysis of Arrhenius rate is not required. In general, considering the length of the combustion section, the residence time for combustion process

is sufficiently long to achieve chemical equilibrium (Ref 30).

To simplify computational analysis, some studies consider only the expansion of hot combustion gases through the torch which can be modeled by considering ideal gas and isentropic relations. The primary equations in this case are (Ref 31),

$$\frac{P_0}{P} = \left[1 + \frac{1}{2}(\gamma - 1)M^2\right]^{\frac{\gamma}{\gamma-1}} \quad \text{(Eq 13)}$$

$$\frac{\rho_0}{\rho} = \left[1 + \frac{1}{2}(\gamma - 1)M^2\right]^{\frac{1}{\gamma-1}} \quad \text{(Eq 14)}$$

$$\frac{T_0}{T} = \left[1 + \frac{1}{2}(\gamma - 1)M^2\right] \quad \text{(Eq 15)}$$

where P, T and ρ are pressure, temperature and density, respectively. Subscript "0" denotes stagnation conditions and γ is specific heat ratio. The velocity of the gas phase (v) can be calculated by considering local Mach number (M) from

$$v = M[\gamma P/\rho]^{1/2} \quad \text{(Eq 16)}$$

The Mach number (M) can be found using area ratio. This equation takes the form (Ref 31),

$$\frac{A_1}{A_2} = \frac{M_2}{M_1}\left[\frac{1 + \frac{1}{2}(\gamma - 1)M_1^2}{1 + \frac{1}{2}(\gamma - 1)M_2^2}\right]^{(\gamma+1)/2(\gamma-1)} \quad \text{(Eq 17)}$$

where A_1 and A_2 are cross-sectional area of two points and corresponding Mach numbers are M_1 and M_2. The mass flow rate of the gas can be calculated using the equation (Ref 31),

$$\dot{m}_g = \frac{P_0}{\sqrt{T_0}} A_t \left[\gamma \frac{\bar{M}_{pr}}{R} \cdot \left(\frac{2}{(\gamma - 1)}\right)^{\left(\frac{\gamma+1}{\gamma-1}\right)}\right]^{1/2} \quad \text{(Eq 18)}$$

Here, $\bar{M}_{pr}$ is average molecular weight of the gas phase and R is the universal gas constant. A_t is the throat area of the torch (Ref 31).

Depending on the equivalence ratio of fuel and oxygen mixture, the product gases attain a high temperature (Ref 32). In case of gaseous fuel like propylene, the complete global chemical reaction can be written as, $C_3H_6 + 4.5O_2 = 3CO_2 + 3H_2O$. At high temperatures attained in oxy-fuel combustion, significant dissociation of species can occur and chemical equilibrium composition contains species other than the complete combustion products. Figure 8 shows the adiabatic flame temperature variation as a function of mixture equivalence ratio (fuel-oxygen ratio divided by the stoichiometric fuel-oxygen ratio) at three different mixture pressures. It is found that the peak temperatures are shifted slightly to fuel-rich conditions and temperatures increase with higher chamber pressures.

Depending on the torch design, Mach number of the gas flow can reach up to 2 at the exit plane of the nozzle. Different types of nozzles can be operated at different pressure ratios making the emerging gas jet over-expanded, expansion matched or under-expanded (Ref 27).

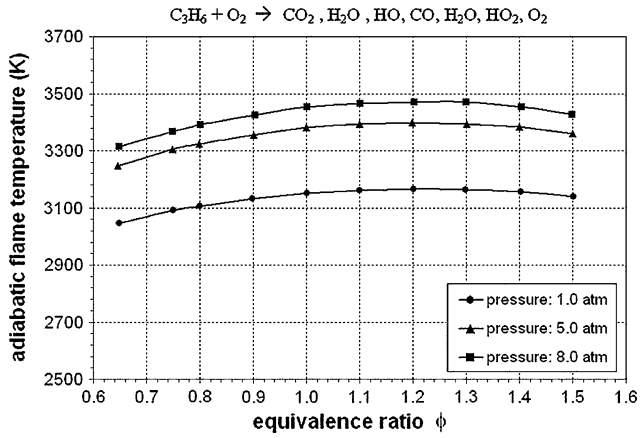

Fig. 8 Computed chemical equilibrium temperatures for propylene-oxygen combustion (Ref 45)

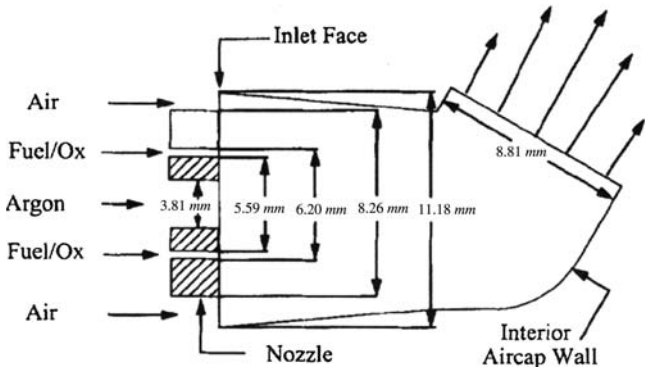

Fig. 9 Schematic of the interior of the three-dimensional HVOF thermal spray torch (Ref 33)

After exiting the nozzle, the gas expands in the atmosphere entraining stagnant ambient air. Depending on the control parameters like mass flow rate and torch design, shock diamonds may or may not be present inside or outside the nozzle.

Hassan et al. (Ref 33) presented a three-dimensional gas dynamics model of HVOF process. In this work, the authors used a 3D computational model to analyze the gas dynamics of a Metco Diamond Jet rotating wire torch. The dimensions of the torch are shown in Fig. 9. Commercial CFD code (CFD-Ace) was used to solve a pressure-based Favre-averaged Navier-Stokes equations to predict the gas flow field with k-ε model for turbulence closure. The combustion modeling used an approximate, one-dimensional equilibrium chemistry code to formulate a single step reaction of propylene and calculation of equilibrium composition. From the reported results, it was found that the temperature of the combustion chamber reaches as high as 3150 K. The Mach number contour plots suggest that near the sharp corner of the torch, flow separation occurs, while near the axis of the

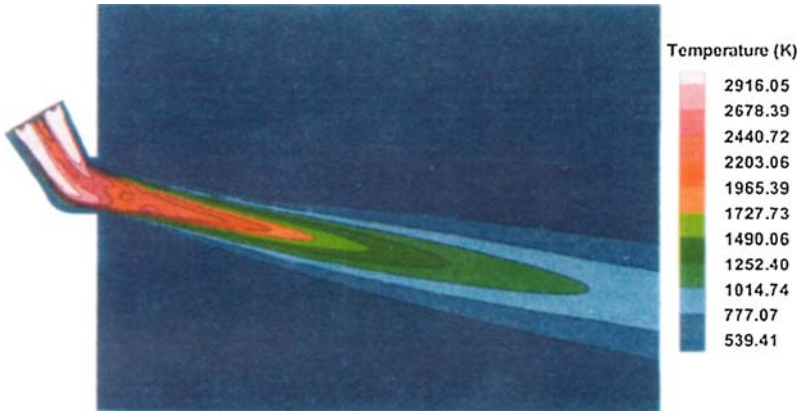

Fig. 10 Gas temperature contour in the plane of symmetry of the aircap and exterior (Ref 33)

flow field, Mach number increases to as high as 1.3. Figure 10 shows the temperature profile outside the nozzle. The temperature of the flow field exhibits decay after the nozzle exit. The gas issuing out of the nozzle expands through a series of shock waves known as shock diamonds. The entrainment of surrounding air ensures mixing of hot gases with cold atmosphere, resulting in a rapid decay of velocity and temperature of the gases. Though the maximum temperature of the gases at the exit of the nozzle is around 2500 K, it cools down to 900 K at the substrate location.

Among others, Gu et al. (Ref 32) also presented a comprehensive CFD model of the gas phase. In this work, the authors used a 2D computational model to study the gas dynamics phenomena involved in the HVOF coating processes. The model assumes a steady state, highly turbulent, fully compressible, high speed flow following combustion in the chamber. The key objective of the model was to analyze the effect of equivalence ratio on the gas dynamics of the combustion products. Initially, the model reported a baseline case with flow rates values of 150, 555 and 35 scfh respectively for fuel (C_3H_8), O_2 and carrier gas (N_2). The inlet temperature was considered to be 288 K. Under this baseline condition, the flow had an equivalence ratio of 0.8 making the flame fuel-lean. The streamlines of the gas phase inside the combustion chamber depict that the gas tends to flow from the wall toward the center of the torch and subsequently accelerate toward the nozzle. The isotherms within the combustion chamber show that the temperature increases to as high as 3180 K. The isotherms also confirm that the highest temperature zones are centered near the fuel/oxygen inlet while the powders and carrier gas remain in comparatively cooler zone. Figure 11 (Ref 32) represents the iso-Mach number contours from the exit of the nozzle, which is marked as $x = 0$ in the figure. It shows that the flow is under-expanded. Simulation also predicted few shock waves, downstream of the nozzle. The authors systematically varied the gas flow rates and equivalence ratio to understand the effect of these parameters on the gas dynamics. The simulations showed that for constant gas

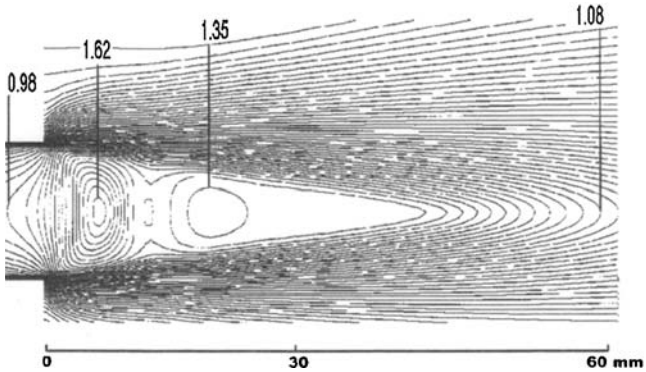

Fig. 11 Iso Mach number lines at the downstream of nozzle. $X = 0$ corresponds nozzle exit (Ref 32)

flow rate, the maximum temperature attained by the combustion products changes with equivalence ratio. Globally the results also depicted that with higher gas flow rate the temperature also increases. Figures 12 and 13 (Ref 32) show temperature and velocity profiles along the centerline for different flow conditions of air-fuel ratios with total flow rates indicated in parentheses. It appears that the flow rates do not have much effect on the centerline temperature and velocity. However, the maximum velocity was attained for the condition corresponding to the highest gas flow rate and fuel-rich flame. On the other hand, with lowest gas flow rate and leanest flame, lowest velocity was attained. Pressure profile along the centerline for different flow conditions shows that within the nozzle, the pressure is as high as 2 to 3 atm, which indicates the need of pressurized feeding of powders. At the exit of the nozzle, the pressure is around 5×10^4 Pa above atmospheric, suggesting that the flow is under-expanded. It was also noticed that the pressure increases with increase in gas flow rate. However, the change in equivalence ratio did not have much effect on the pressure field.

The authors (Ref 32) also performed a study on the effect of torch design on the gas-dynamics. The simulations showed that with shorter span of combustion

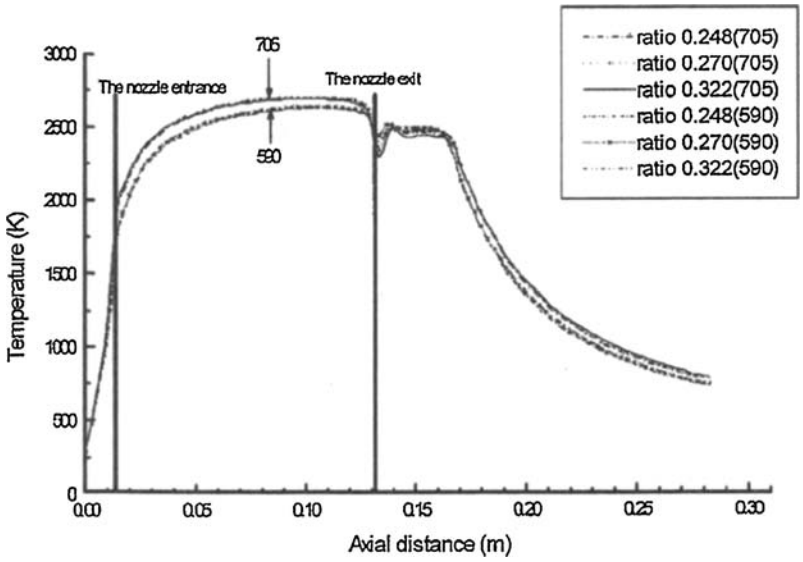

Fig. 12 Variation of gas temperature with distance along the centerline (symmetry axis) of the computational domain for different gas ratio at flow rates of 590 and 705 scfh (Ref 32)

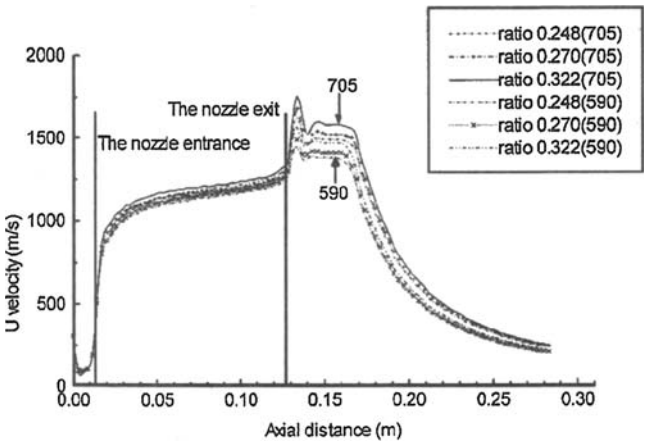

Fig. 13 Variation of gas velocity with distance along the centerline (symmetry axis) of the computational domain for gas ratios, shown at flow rates of 590 and 705 scfh (Ref 32)

chamber, the particles have shorter time to accelerate, which will result in longer residence time. Although the gas temperature decreases slightly with shorter combustion chamber length, the slow moving particles tend to be heated for longer time, increasing the possibility of oxidation before reaching the substrate.

4. Modeling of Particle or Droplet Heat-up

Once the thermal and flow fields of a DC-arc plasma or HVOF jet are computed, these results can be utilized to determine particle or droplet heat-up behavior. In the case of particle injection, the particles attain different velocities and temperatures before impacting on a substrate depending on the particle loading rate, injection location, particle properties, size distribution and effects of turbulent transport. In case of solution precursor droplets, the droplets undergo precipitation and shell formation followed by shell rupture as described earlier. Eventually depending on the initial droplet size and concentration of solute in the droplet, they become fully pyrolized or remain in un-pyrolized condition.

In this study, it is realized that the aerodynamic processes of very short timescale have already produced droplets of stable sizes that will not undergo further breakup. All the droplets introduced into the plasma undergo rapid heating resulting in solvent vaporization and increased concentration of solute near the droplet surface. At a critical value of solute concentration, precipitation occurs, resulting in the formation of a solid shell around the liquid core. The precipitation leading to shell formation is assumed to be instantaneous based on the supersaturation concentration value of the solute based on the literature data (Ref 34, 35). The binary (solute + solvent) droplets are assumed to be injected axially or transversely into a high-temperature plasma jet where solvent portion of the droplet vaporizes with simultaneous reduction in droplet size and increase in the solute concentration. The droplets are assumed to be composed of precursor (solute) dissolved in a solvent with a prescribed initial precursor mass fraction. Droplet motion in the hot convective gas environment is governed by the droplet momentum equation given by (Ref 36, 37),

$$\frac{\partial U}{\partial t} = \frac{3C_D}{8r_s}\frac{\rho_\infty}{\rho_L}|U_\infty - U|(U_\infty - U) \qquad \text{(Eq 19)}$$

$$\frac{\partial V}{\partial t} = \frac{3C_D}{8r_s}\frac{\rho_\infty}{\rho_L}V^2 \qquad \text{(Eq 20)}$$

where U, V are the droplet velocities in x and y directions, C_D is the drag coefficient due to the relative motion

between the droplet and the surrounding hot gases with U_∞ being the streamwise local plasma flow velocity. The change in the droplet radius is given by,

$$\frac{dr_s}{dt} = -\frac{\dot{m}}{4\pi\rho_L r_s^2} \quad \text{(Eq 21)}$$

where $\dot{m}$ is the mass rate of vaporization, ρ_L is the liquid density and r_s is the radius of the droplet. The drag coefficient, C_D, is modified for the surface blowing effects as follows,

$$C_D = \frac{24}{Re(1+B_M)} \quad \text{(Eq 22)}$$

where B_M is the Spalding's mass transfer number. The mass vaporization rate, $\dot{m}$, can be expressed in terms of either mass or heat transfer as (Ref 36, 37),

$$\dot{m} = 2\pi\rho_g D_{12} r_s Sh^* \ln(1+B_M) \quad \text{(Eq 23a)}$$

$$\dot{m} = 2\pi\frac{k_g}{C_{P,v}} r_s Nu^* \ln(1+B_T) \quad \text{(Eq 23b)}$$

In these equations, Nusselt number Nu^* and Sherwood number Sh^* are based on a nonvaporizing sphere and modified for vaporization effects because of the varying film thickness around the droplet. When the mass vaporization rate from Eq 23a and 23b are equated, a relationship between the droplet surface temperature and surface solute vapor concentration just above the liquid surface is obtained. This relationship along with a thermodynamic relation for vapor-liquid equilibrium (Clapeyron equation) and the Rault's law for the mixture facilitate the iterative solution for the droplet surface vapor mass fraction and temperature. These quantities are calculated at each step along the droplet trajectory and coupled with the solution of species and energy equations within the droplet.

Within the droplets, the energy and species transport are computed to determine the distributions of these quantities. The most detailed transport within the droplet includes the effects of convection induced by the shear at the liquid-gas interface on the droplet surface. This shear induces an internal recirculatory flow within the droplet that is characterized by a spherical Hill's vortex whose strength is computed as a function of the slip velocity between the droplet and the gas stream. The general form of the species and energy equations accounting for the internal recirculation can be written in spherical polar coordinates and nondimensional form as (Ref 36, 37),

$$Le_L \bar{r}_s^2 \frac{\partial \bar{\chi}_z}{\partial \tau} + \left(0.5 Pe_L Le_L \bar{V}_r \bar{r}_s - Le_L \beta\eta\right)\frac{\partial \bar{\chi}_z}{\partial \eta} + 0.5 Pe_L Le_L \frac{\bar{V}_\theta \bar{r}_s}{\eta}\frac{\partial \bar{\chi}_z}{\partial \theta} = \frac{1}{\eta^2}\frac{\partial}{\partial \eta}\left(\eta^2 \frac{\partial \bar{\chi}_z}{\partial \eta}\right) + \frac{1}{\eta^2 \sin\theta}\frac{\partial}{\partial \theta}\left(\sin\theta \frac{\partial \bar{\chi}_z}{\partial \theta}\right) \quad \text{(Eq 24a)}$$

and

$$\bar{r}_s^2 \frac{\partial \bar{T}}{\partial \tau} + \left(0.5 Pe_L \bar{V}_r \bar{r}_s - \beta\eta\right)\frac{\partial \bar{T}}{\partial \eta} + 0.5 Pe_L \frac{\bar{V}_\theta \bar{r}_s}{\eta}\frac{\partial \bar{T}}{\partial \theta} = \frac{1}{\eta^2}\frac{\partial}{\partial \eta}\left(\eta^2 \frac{\partial \bar{T}}{\partial \eta}\right) + \frac{1}{\eta^2 \sin\theta}\frac{\partial}{\partial \theta}\left(\sin\theta \frac{\partial \bar{T}}{\partial \theta}\right) \quad \text{(Eq 24b)}$$

subject to the initial and boundary conditions,

$$\tau = 0 \rightarrow \bar{\chi}_z = 0 \quad \text{and} \quad \bar{T} = 0$$

$$\eta = 1 \rightarrow \frac{\partial \bar{\chi}_z}{\partial \theta} = 0; \int_0^\pi \frac{\partial \bar{\chi}_z}{\partial \eta}\sin\theta\, d\theta = \frac{\dot{m}}{2\pi r_s \rho_L D_{za} \chi_{z,o}}$$

$$\text{and} \quad \frac{\partial \bar{T}}{\partial \theta} = 0; \int_0^\pi \frac{\partial \bar{T}}{\partial \eta}\sin\theta\, d\theta = \frac{\dot{Q}}{2\pi r_s k_L T_0}$$

$$\theta = 0,\ \pi \rightarrow \frac{\partial \bar{\chi}_z}{\partial \theta} = 0 \quad \text{and} \quad \frac{\partial \bar{T}}{\partial \theta} = 0$$

The boundary conditions at the droplet surface ($\eta = 1$) correspond to uniform droplet surface temperature (i.e. $T_s = T_s(t)$) and the total heat flux received by the droplet at its surface. All the symbols are defined in the nomenclature.

Some sample results are shown in Fig. 14 for a 20 μm droplet injected into DC-arc plasma at two time instants along its trajectory (Ref 36). It is seen that the internal circulation inside the droplet can result in significant solute concentration and in moderate temperature variations. Such data are needed when solute precipitation in the droplets is to be predicted. Sometimes, the computational overhead to compute the internal droplet temperature and concentration variations may not be justified particularly for those cases where many droplet calculations are needed to develop statistics. In such cases, spherically symmetric model without internal droplet circulation can be utilized. In this case, the governing equations reduce to (Ref 38, 39):

$$Le_L \bar{r}_s^2 \frac{\partial \bar{\chi}_z}{\partial \tau} - 0.5 Le_L \frac{dr_s}{dt}\eta\frac{\partial \bar{\chi}_z}{\partial \eta} = \frac{1}{\eta^2}\frac{\partial}{\partial \eta}\left(\eta^2 \frac{\partial \bar{\chi}_z}{\partial \eta}\right) \quad \text{(Eq 25a)}$$

$$\bar{r}_s^2 \frac{\partial \bar{T}}{\partial \tau} - 0.5\frac{dr_s}{dt}\eta\frac{\partial \bar{T}}{\partial \eta} = \frac{1}{\eta^2}\frac{\partial}{\partial \eta}\left(\eta^2 \frac{\partial \bar{T}}{\partial \eta}\right) \quad \text{(Eq 25b)}$$

with the initial and boundary conditions as,

$$\left\{\begin{array}{c}\bar{\chi}\\ \bar{T}\end{array}\right\}(\tau = 0) = 0 \quad \text{and} \quad \frac{\partial}{\partial \eta}\left\{\begin{array}{c}\bar{\chi}\\ \bar{T}\end{array}\right\}\Bigg|_{\eta=0} = 0$$

$$\text{and} \quad \frac{\partial}{\partial \eta}\left\{\begin{array}{c}\bar{\chi}\\ \bar{T}\end{array}\right\}\Bigg|_{\eta=1} = \left\{\begin{array}{c}\frac{\dot{m}}{2\pi r_s \rho_L D_s \chi_{z,o}}\\ \frac{\dot{Q}_L}{2\pi r_s k_k T_0}\end{array}\right. \quad \text{(Eq 26)}$$

where $\dot{Q}_L$ is the heat flux to the droplet, k_L is the liquid conductivity, ρ_L is liquid density, D_s is the mass diffusivity of solute in solvent.

The models described above allow the computation of the solute concentration and temperature within the droplets. This information is needed for determination of

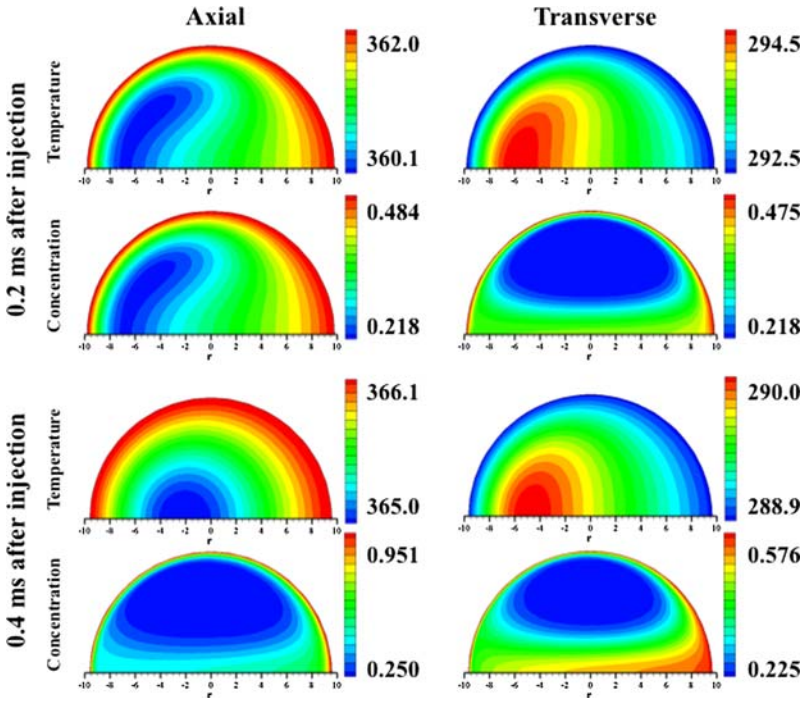

Fig. 14 Temperature and solute concentration distributions within a 20 μm diameter droplet injected into a DC-arc plasma from Ref 36

the precursor precipitation time and the regions of the droplets that undergo precipitation. Clearly, this requires a model of precipitation kinetics and is probably the weakest link in modeling of the liquid precursor based thermal spray modeling. The current state of knowledge in precipitation of liquid precursors is discussed in the next section of this paper. It is however predicted that droplets can undergo precipitation near their surface due to concentration of the solute there and this causes shell-type particle morphologies to form.

Subsequent to shell formation, further heating of the particle containing a liquid core can lead to either venting of the vapor inside the shell if the shell is porous or internal pressurization and eventual rupture of the shell. This portion of the process can be modeled as follows. The particle motion through the hot plasma is still governed by Eq 19 and 20 except that the particle size is now fixed at the outer diameter of the precipitate shell. The Nusselt number for the porous and nonporous shells is obtained as described in Basu and Cetegen (Ref 38). The model for the particle interior is divided into three zones: solid shell, liquid core and vapor annulus. In each region, the energy equation is of the same form as Eq 25 with a moving interface between the liquid core and the vapor film. The enthalpy carried by the vapor escaping through the pores is accounted for in the model as detailed in Basu and Cetegen (Ref 38). Depending on the type of shell formed, one may or may not have any venting effect through the pores in the shell. However, for the general case of a shell porosity (ε), one can write the following mass balance equation for the vapor.

$$\dot{m}_v = -\dot{m}_l - \dot{m}_{out} \quad \text{(Eq 27)}$$

where $\dot{m}_v$ is the vapor mass generation rate within the shell, $\dot{m}_l$ is the rate of change remaining core liquid mass and $\dot{m}_{out}$ is the rate of vapor mass leaving the porous shell. After some algebraic manipulations with the ideal gas law assumption, this reduces to:

$$\frac{dp_v}{dt} = \frac{RT_v}{V_v}\left[4\pi r_l^2 \rho_v \left|\frac{dr_l}{dt}\right| - 4\pi r_l^2 \rho_l \frac{dr_l}{dt} - \rho_v A_{pore} V_{pore}\right] \quad \text{(Eq 28)}$$

where V_{pore} is the velocity of the gas venting through the pores of the shell estimated from Karman-Cozeny equation while A_{pore} is the total area of the pores. ρ_v and ρ_l denote the densities of the vapor and liquid phase while r_l is the radius of the liquid core. Equation 28 gives an expression for internal pressure rise as a function of the vapor velocity escaping through the pores and the rate at which the liquid front is receding toward the droplet center. Internal pressurization of the shell due to vaporization of the liquid within it can lead to shell rupture or inflation depending on the shell type that forms during precipitation. This obviously depends on the solute and solvent characteristics and the thermo-physical conditions under which the precipitation occurs.

The interaction between particle and gas phase can be modeled similarly by solving momentum and energy equation for the particle phase. The primary governing equations for the particles in Lagrangian form are (Ref 31),

$$m_p \frac{dv}{dt} = \frac{1}{2} C_D \rho_g A_P (v_g - v_p)|v_g - v_p| \quad \text{(Eq 29)}$$

$$\frac{dx_p}{dt} = v_p \quad \text{(Eq 30)}$$

$$m_p C_{p_p} \frac{dT_p}{dt} = \begin{Bmatrix} hA'_{s_p}(T_g - T_p) + S_h & (T_p \neq T_m) \\ 0 & (T_p = T_m) \end{Bmatrix} \quad \text{(Eq 31)}$$

$$\Delta H_m m_p C_{p_p} \frac{df_p}{dt} = \begin{Bmatrix} hA'_{s_p}(T_g - T_p) + S_h & (T_p = T_m) \\ 0 & (T_p \neq T_m) \end{Bmatrix} \quad \text{(Eq 32)}$$

Here subscripts p, g and m stand for particle, gas phase and melted phase respectively. m is the mass, t is time, C_D is drag coefficient, v is axial velocity, x is axial distance, A_s is surface area, C_p is specific heat and constant pressure. f is the fraction of molten mass. S_h is source term for radiative heating. In case where radiation is neglected, $S_h = 0$. The convective heat transfer coefficient can be calculated by correlations. Most of the researchers use, Ranz-Marshal relation given by $h = k_g/d_p(2 + 0.6Re^{1/2}Pr^{1/3})$. Reynolds number and Prandtl number in this case are defined as, $Re = \rho_g d_p|v_p - v_g|/\mu_p$ and $Pr = C_{pp}\mu_p/k_g$. k_g is thermal conductivity of the gas phase and d_p is the diameter of the particle. Solving these equations coupled with the gas phase (described earlier) results in the instantaneous velocity and temperature of the particle (Ref 31).

5. Precursor Chemistries and Precipitation Kinetics for Liquid Precursors

The weakest link in the modeling of liquid precursor based thermal spray process is the detailed description of the precipitation of solute in a droplet. Currently, the spray pyrolysis literature contains the most extensive studies. Both experimental and modeling studies explored conditions under which different types of particles are formed. Zhang et al. (Ref 40) and Jain et al. (Ref 41) reviewed this subject presenting both experimental data and modeling results pointing to the different morphologies. Che et al. (Ref 42) carried out studies in which the particle structure was controlled by reactions within the droplets in spray pyrolysis. They achieved dense or hollow single crystal or layered particle structures by carefully controlling the reactions within droplets, sintering and phase transformations. Zhang et al. (Ref 40) studied experimentally the formation of zirconia from different zirconium salts and determined the conditions and precursor solutions that yield solid particles. Nimmo et al. (Ref 43) studied generation of zirconia from zirconium nitrate sprayed with a diameter of less than 5 μm into a controlled heating furnace. They were able to produce tetragonal phase ultrafine zirconia powers under certain operating conditions.

Linn and Gentry (Ref 44) performed an experimental study of single droplet precipitation of different aqueous solutions of calcium acetate, sodium acetate, sodium carbonate, ammonium chloride, lithium manganous nitrate and barium alumino silicate. They found that after a period of uniform shrinkage due to evaporation in a hot gas environment, crystallization, crust formation and fracture of the crust were observed. Ammonium chloride and lithium manganous nitrate showed bubbling and inflation of the precursor droplets after the initial shrinkage. While these studies illustrate the different nucleation mechanisms and in some cases inflation of droplet upon heating, these experiments were conducted at low heating rates where droplets were suspended in a relatively low gas temperature environment (with respect to flame or a plasma) and low velocities. Since the precipitation morphology is strongly dependent on the droplet heating rates, the actual processes taking place in a droplet can be altered significantly. Modeling of precipitation of solute salts in a liquid droplet has been primarily based on the homogeneous nucleation hypothesis (Ref 34, 35). It is assumed that onset of precipitation occurs when the solute concentration reaches a supersaturation level and engulfs all regions of the droplet that exceed the equilibrium saturation concentration. While fundamental studies of precipitation onset in solution droplets have been undertaken (Ref 34, 35), these studies have revealed that the parameters affecting the precipitation onset are difficult to determine even for the simple single component solutions under well-controlled conditions. Models based on the minimization of the Gibbs energy have been considered to predict the onset of precipitation. In practice, validity of homogeneous precipitation hypothesis is in question firstly due to the more likely possibility of the heterogeneous precipitation as a result of impurities and secondly because of the effects of very rapid heating of droplets.

Precipitation of the solute salts in these and other models is based upon attainment of super-saturation concentration of the solute before the onset of precipitation followed by precipitation in all regions of the droplet that are above the equilibrium saturation concentration. This assumption of homogeneous precipitation has been used widely in modeling, yet its validity for different material systems and droplet heating conditions is not known. Ozturk and Cetegen (Ref 36) and Basu and Cetegen (Ref 38, 39) used this concept of homogenous precipitation in their models and showed that large droplets typically form shell type precipitates, which are detrimental to the final coating quality as they are embedded as unmolten fragments in the coating. Smaller droplets are not only better entrained but tend to volume precipitate. This volume precipitation and subsequent intense heating usually results in molten splats on the substrate resulting in denser coatings. Some sample results are shown in Fig. 15 (Ref 36).

6. Modeling of Coating Deposition Process

The coating generation process is an interaction between molten droplet/particle and substrate surface or

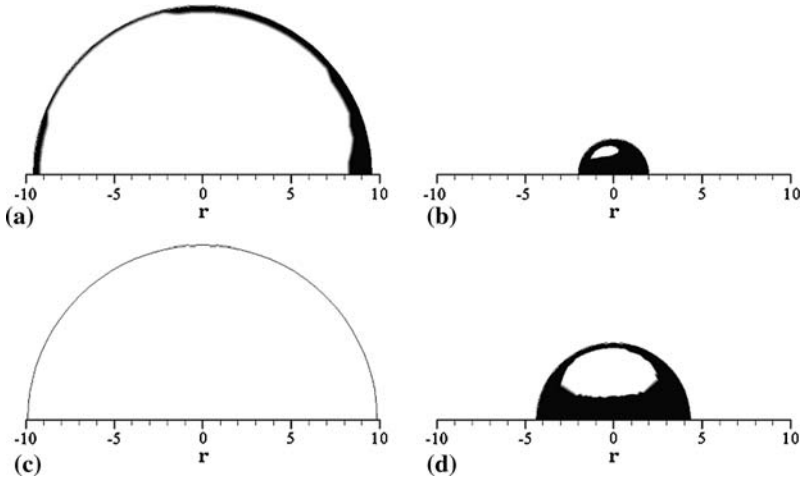

Fig. 15 Precipitation zones within the droplets for (a) axially injected 20 μm droplet 0.4 ms after injection, (b) transversely injected 20 μm droplet 0.4 ms after injection, (c) axially injected 5 μm droplet 0.2 ms after injection, and (d) axially injected 10 μm droplet 0.36 ms after injection (Ref 36)

previously deposited materials on the surface. This interaction is also responsible for porosity development in the coating. Most of the models dealing with coating evolution assume that the coating generation is a consequence of individual molten droplet splats impacting the surface independently. The temperature, velocity and size of particles determine thickness of each splat which dictates the coating density. The size of particles before impact can be expressed as a distribution function (Ref 31),

$$f(d_p) = \frac{1}{\sqrt{2\pi}\sigma d_p}\exp\left(-\frac{(\ln(d_p)-\mu)^2}{2\sigma^2}\right),$$

where μ, σ^2 are two parameters corresponding mean and variance of $\ln(d_p)$. Most of the available works also assume that a particle after impacting the substrate takes shape of a flattened cylinder and the flatness can be expressed by,

$$\xi = \frac{D_s}{d_p} = \frac{2}{d_p}\sqrt{\frac{A_s}{\pi}},$$

where D_s is the diameter of the splat and A_s is the surface of the splat. Considering the volume conservation, the height of the splat can also be calculated (Ref 31). The flattening factor (ξ) depends on many parameters like, Reynolds number, Peclet number and Weber number. However, many researchers used a simplified formulation, $\xi = 1.2941 Re^{0.2}$. Simulation of these parameters for each and every droplet results in a stochastic coating pattern (Ref 31).

7. Some Results from Previous Studies

In this section, some results from previous studies are highlighted for plasma and HVOF flame jet thermal spray processes. Figure 16 shows some sample results from Yu (Ref 45) on particle velocities and temperatures for different particle sizes in a DC-arc plasma as determined from experiments. Clearly large variations of particle temperatures, velocities and sizes exist in thermal spray processes and these contribute to the microstructural features of the deposited coatings. In addition to the particle state variations, variation of particle trajectories within a plasma jet leads to dispersion of particle positions at different jet cross sections as shown in Fig. 17 (Ref 16). Dispersion is also affected by the degree of swirl as swirling flow has a tendency to have a larger degree of dispersion at farther downstream positions as shown in this figure as well. Figure 18 shows the effects of particle carrier gas flow rate on particle trajectories, velocities, temperatures and vaporization rates (Ref 21). The particle penetration into the plasma increases with increasing carrier gas flow rate and peak particle temperatures are also higher for the higher carrier gas flow rates employed in this study. There is typically an optimum carrier gas flow rate for particles to penetrate into the plasma jet and undergo sufficient degree of heating in the plasma. Figure 19 (Ref 25) shows another example of particle heating in a DC-arc plasma. In this case, a 30 μm zirconia particle is injected into a DC-arc plasma. Both surface and core temperature evolution is shown on the left panel. The internal particle temperature rises with increasing time within the particle as shown on the right panel.

An important aspect of particle heat-up in a plasma or HVOF flame jet is the treatment of heat transfer from the gas stream into the particle or droplet. As mentioned earlier, noncontinuum effects may be prevalent in some cases. Figure 20 (Ref 19) shows the ratio of heat fluxes with and without the Knudsen effect in the conduction regime. While the noncontinuum effects may not be significant for larger diameter particles, they can be significant for small particles.

There have not been many studies of droplet injection into plasmas in the past. There are some recent modeling

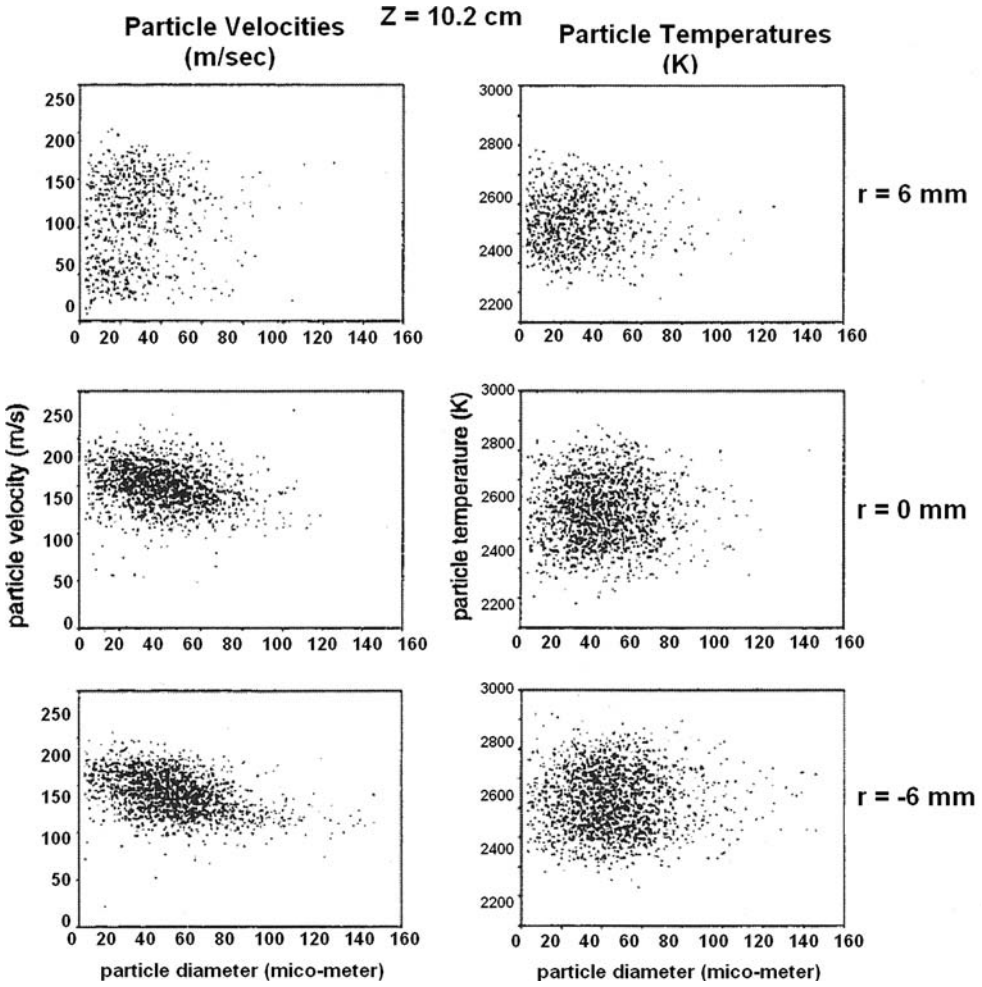

Fig. 16 Particle velocity and temperatures as a function of particle size at an axial distance of 10.2 cm at three radial locations (Ref 45)

studies of liquid precursor droplet injection into plasmas (Ref 14, 36, 38, 39). In these studies, droplet break-up and evolution of solute concentrations within injected droplets were considered. Figure 21 shows the Weber number variations along droplet trajectories in a plasma jet as reported in Ref 14. From the Weber numbers, the propensity of the droplets for break-up is evaluated as high Weber number regions are those where droplet break-up is expected.

Li et al. (Ref 29) performed a computational study on in-flight behavior of particles during HVOF process. The torch shown in Fig. 6 (Ref 29) was designed in such a way that the Mach number at the exit of the nozzle to be around 2. Maximum gas velocity with this nozzle can go up to 2000 m/s. The gas dynamics of the combustion process has been modeled using the similar methodologies as described earlier. The particle heating formulation neglected temperature variation within the particle.

The turbulent nature of the HVOF gas flow field introduces indeterminism with respect to particle tracking and hence a stochastic method was adopted, where instantaneous velocity is always represented as the sum of the average velocity and the fluctuating component of the fluid velocity. Temperature distribution within the flow field shows that the maximum temperature is around 2500 K and it is located in the core of the jet. The velocity profile of the gas field along the radial direction at different axial planes is shown in Fig. 22 (Ref 29). The authors also reported the effect of injection location on particle velocity. Figure 23 (Ref 29) depicts the axial velocity profiles of five different sized particles injected from different locations. The results showed that despite being injected at different axial locations, the same sized particles always attain similar velocities and temperatures before impacting on the substrate. The authors in this work also performed a statistical analysis of the distribution of particle impact velocity and temperature for a wide range of particle sizes and injection locations. The analysis depicted that 90% of the total volume of particles impact the substrate within a 2 mm radius from the center. Residence times of the particles were around 2 to 4 ms, while the axial velocity and temperature at the time of impact were around 94 m/s and 1176 K, respectively.

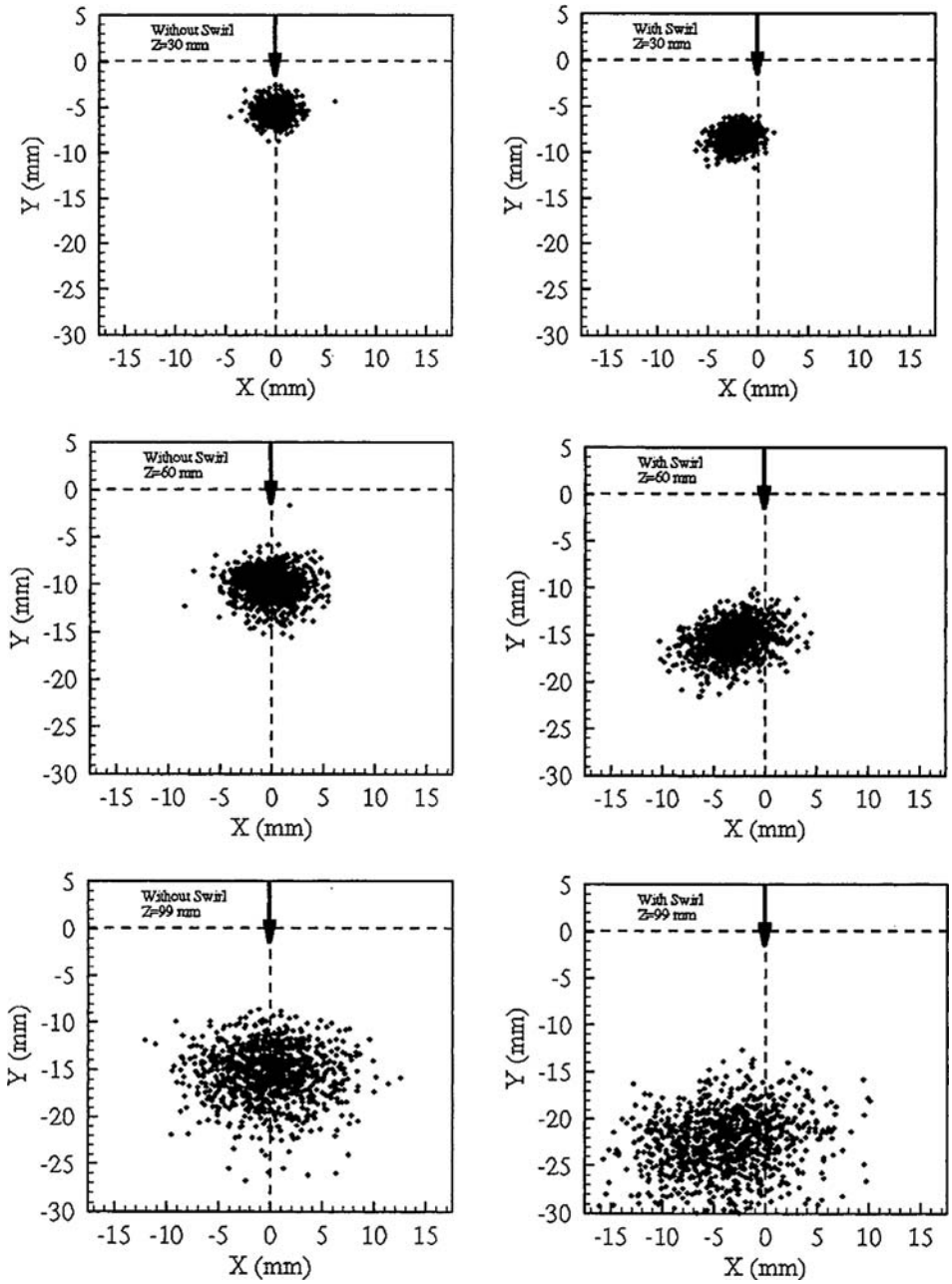

Fig. 17 Comparison of the predicted particle distributions at three successive sections with and without swirl from Ref 16

Bartuli et al. (Ref 46) conducted a detailed parametric study for liquid fuel HVOF process for nano WC reinforced cobalt coating. For assessing the effect of spray parameters on the microstructure, a computational model was used to simulate the combustion process and interaction of the WC-Co particles with the exhaust gases. Additionally, experimental work was performed to validate the model and compare the coating quality with the conventional micro-sized power coatings. In this work, commercially available spraying equipment (JP-5000, Tafa Inc., Praxair Surface Technologies, Concord, NH) with a kerosene-oxygen mixture as fuel was used for experimentation. For computations, k-ε turbulence model was adopted. Single-step reduced chemistry model was used for the combustion process.

Optimal spraying conditions are found to be functions of parameters like fuel (kerosene) flow rate, length of the torch barrel and spraying distance. The oxygen flow rate was maintained at 2000 scfh. The temperature and velocity distribution of the combustion gas inside the torch for all the different fuel flow rates show that the static temperature of gas phase is highest for a kerosene flow rate of

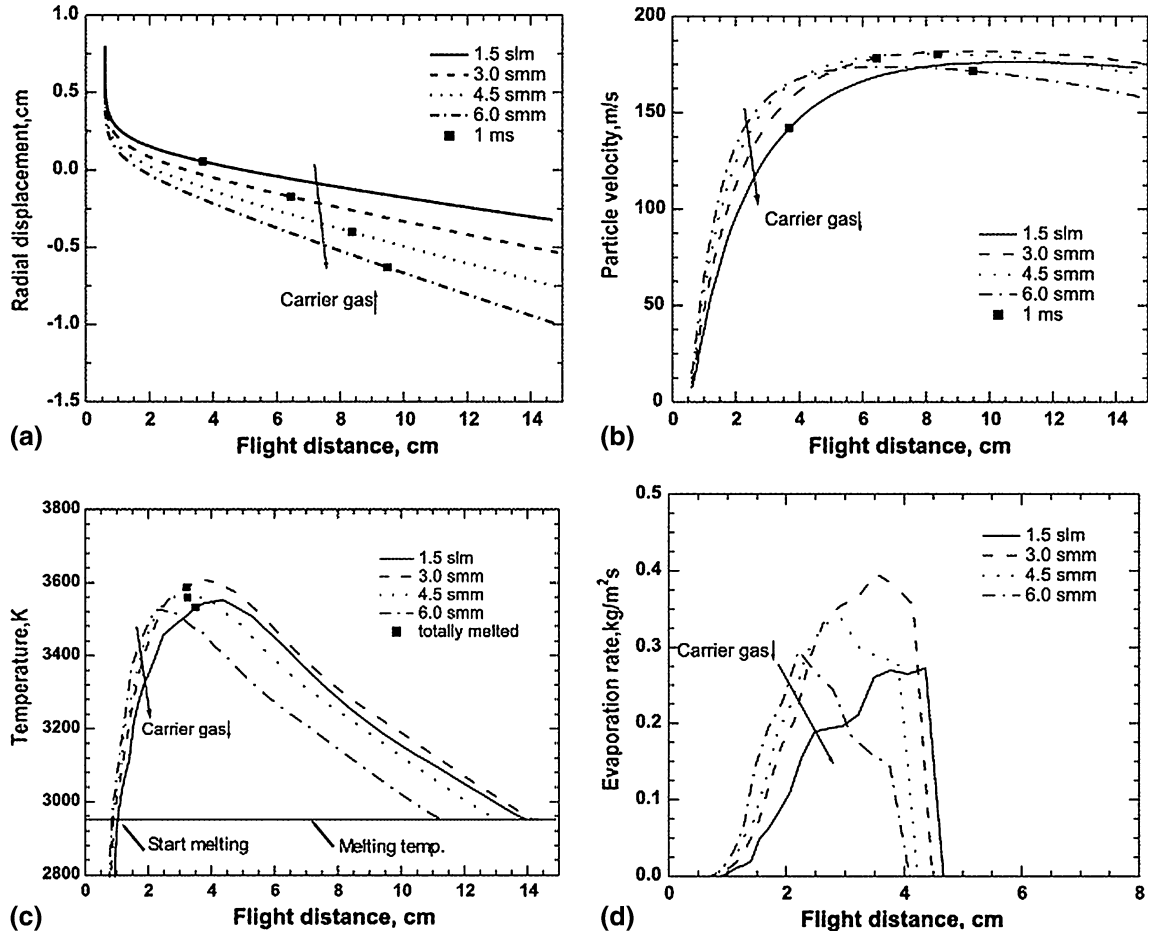

Fig. 18 Dependency of in-flight behavior for zirconia particles of 30 μm as a function of carrier gas flow rates: (a) particle trajectories, (b) particle velocity, (c) particle temperature and (d) evaporation rates from Ref 21

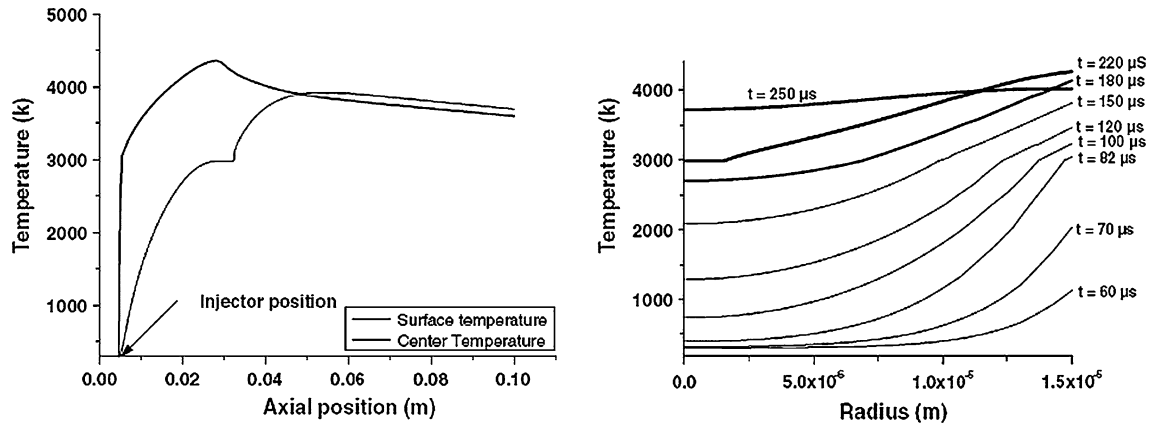

Fig. 19 Axial evolution of zirconia particle temperature and the temperature distribution within the particle at different time instants for a 30 μm particle from Ref 25

6.0 gph while the velocity profile remains largely unaffected. The effect of three different barrel sizes on the particle (WC-Co particles of average size of 48 μm) velocity and temperature was also studied. The simulation results are illustrated in Fig. 24 (Ref 46). The results show that inside the nozzle, longer barrel length leads to higher values of peak velocity and temperature. It is claimed that this information can be utilized for optimization of the

control parameters for minimum thermal interaction of particle and combustion flame reducing the chances of decarburization grain growth leading to adhesive coatings.

Dongmo et al. (Ref 47) performed a detailed computational study to model the HVOF process using alumina (Al_2O_3) powder. They also used commercial Spray-Watch® system to experimentally validate their model. In this work, a 3D model was developed to simulate the combustion and gas dynamics processes during the HVOF process. This model also investigated the interactions of particles and combustion gases. The torch has been modeled as TopGun-G (GTV mbH, Luckenbach, Germany). Similar to most of the models described earlier, this work uses Eulerian and Lagrangian approaches to solve the velocity and temperature fields of the gas and particle fields, respectively. Reynolds and Farve-averaged Navier-Stokes' equations along with k-ε turbulence model were adopted. Commercially available ANSYS-CFX 11 software was used. The parameter values considered for this simulation are stated in Table 1 (Ref 47). In this work, gaseous propane was used as the fuel. The distribution of all the species involved in the combustion process along the centerline is shown in Fig. 25(a) and (b)

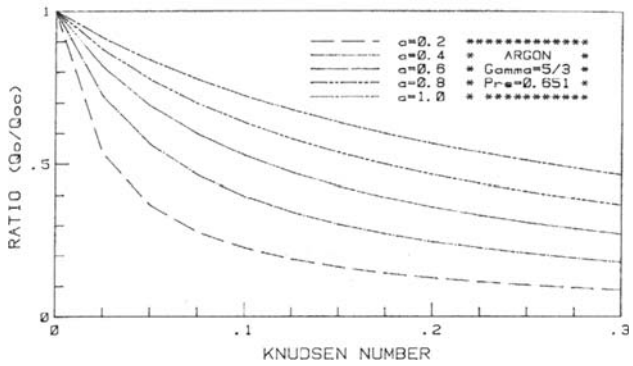

Fig. 20 Heat transfer under noncontinuum conditions (Q_2 with Knudsen effect, Q_0 without Knudsen effect)\(Ref 19)

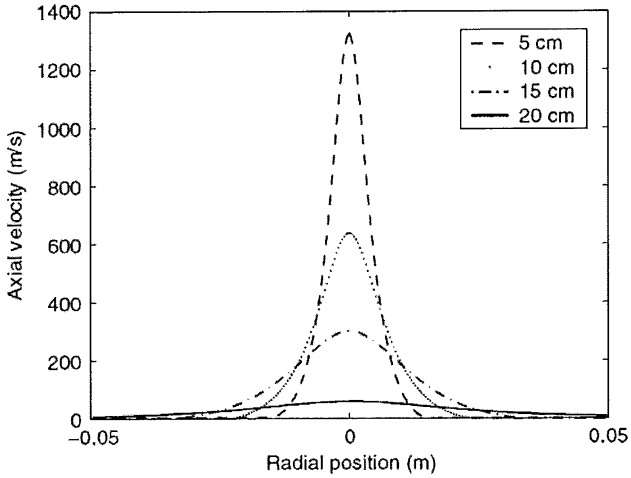

Fig. 22 Velocity distribution of the gas phase along the radial direction at different axial planes (Ref 29)

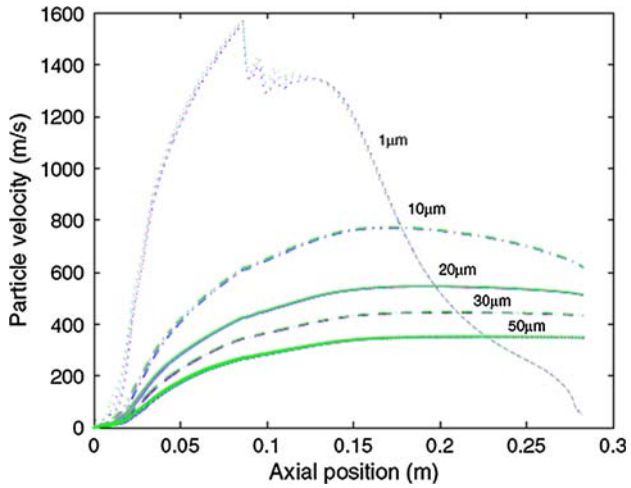

Fig. 23 Profiles of axial velocity of particles of five different sizes injected from different axial locations (Ref 29)

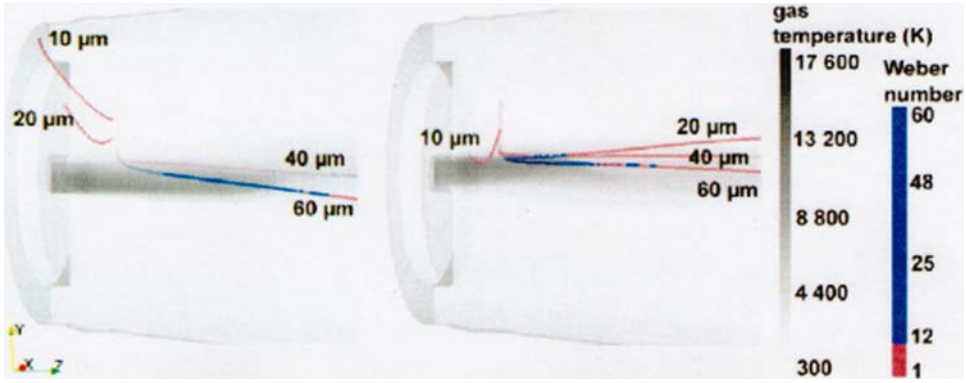

Fig. 21 Variation of Weber number along droplet trajectories of water droplets 20, 40 and 60 µm diameter from Ref 14

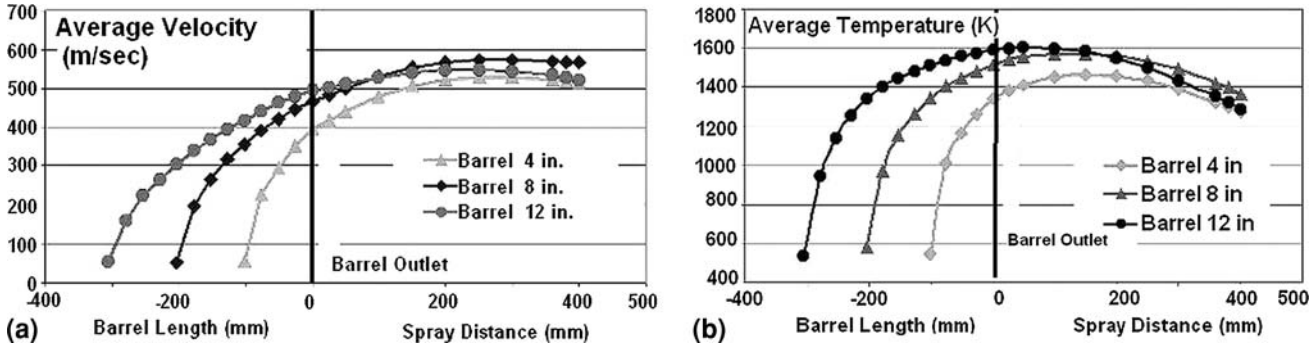

Fig. 24 (a) Average velocity and (b) average temperature profiles of Ref 46 particles (WCCo, 48 μm average size) inside and outside of the barrels of different lengths

Table 1 Parameters for the HVOF computational domain using oxy/fuel ratio 0.8 (Ref 47)

	Inlet C_3H_8/O_2	Inlet N_2	Inlet Al_2O_3	Wall	Free jet	Substrate
Mass flow, g/s	5.143×10^{-3}	2.065×10^{-3}	0.068	…	…	…
Temperature, K	300	300	300	460	298	298
Pressure, Pa	…	…	…	…	10^5	…

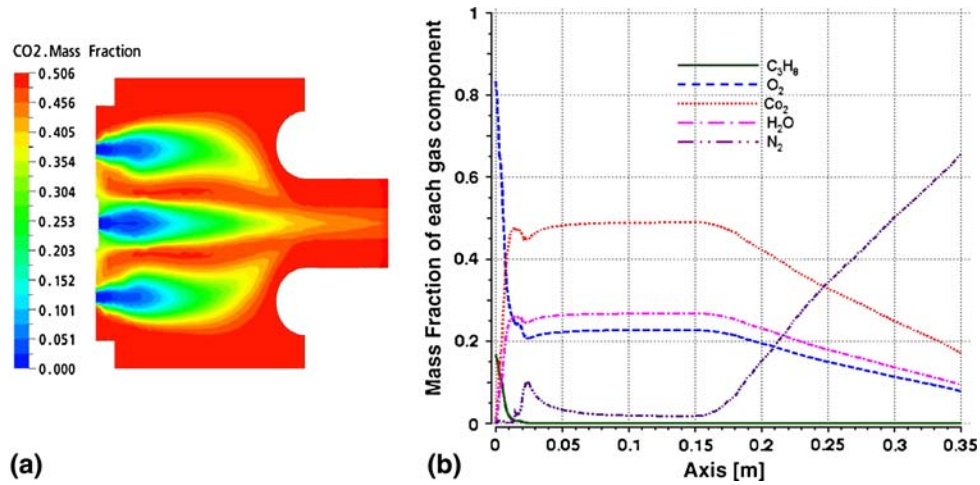

Fig. 25 (a) Mass fraction of the CO_2 within the torch, (b) mass fraction of all the species along the centerline (Ref 47)

(Ref 47). Figure 26 (Ref 47) shows the pressure and Mach number distribution along the centerline inside and outside of the torch. For the converging nozzle, the velocity as well as Mach number of the exhaust gas increases reaching a supersonic level. The simulation results also depicted the presence of diamond shocks. The model also predicted the axial velocities and the temperature for different sized particles. The results depict that particles having sizes smaller than 20 μm undergo rapid decay in velocity and temperature outside the torch. They do not reach the substrate at the point of impact. This finding has also been confirmed by measurements using SprayWatch® system. In summary, the authors put forward a numerical model for HVOF process using propane as fuel and alumina as powder. The results show that the particles of size less than 20 μm are not suitable for coating as their low mass and inertia do not allow them to reach the substrate with desirable velocity and temperature characteristics. Other significant works in this category include the work of Tawfik and Zimmerman (Ref 48) who proposed a one-dimensional single-phase, nonadiabatic frictional flow with variable specific heats to model the flow inside the nozzle of the HVOF torch and the supersonic jet plume outside the nozzle. Though this model is simple in construction, it was validated by a series of experiments and provided a low cost-effective analysis contrary to the more computationally intensive models described earlier. The particle interaction was modeled using a Lagrangian approach with a lumped capacitance model for heat transfer. The fuel used was kerosene with Inconel and WC as the

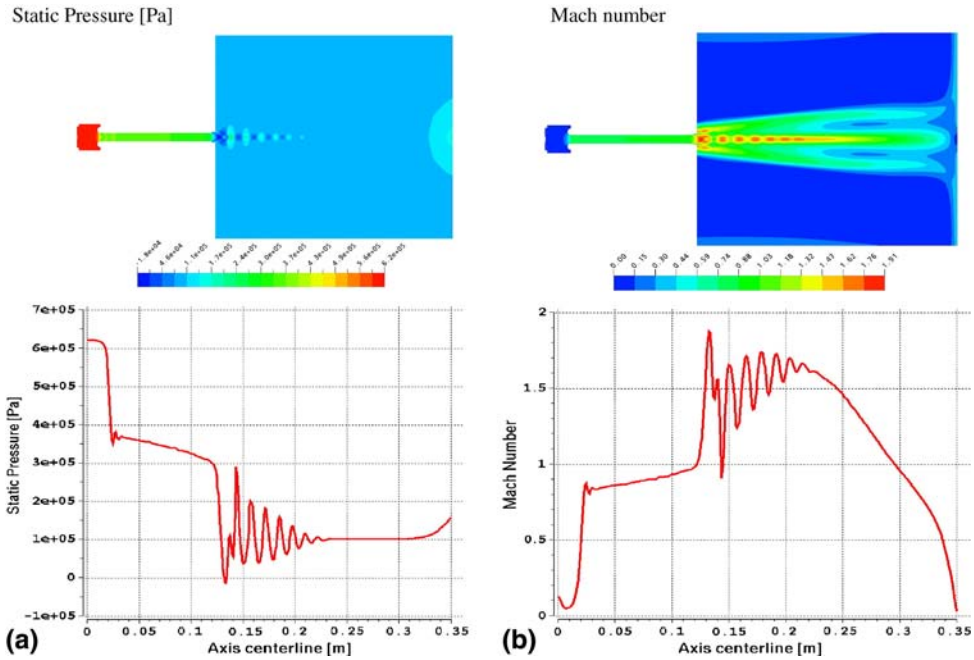

Fig. 26 Contour plots of (a) static pressure and (b) Mach number along the centerline (Ref 47)

injected particles. Their simulations indicated that heat transfer between the gas and the particle is more efficient than momentum transfer resulting in faster rise in particle temperature. Particles for a diameter range of 38-50 μm exhibit a highest temperature of around 2500 R with an average velocity of 3500-5000 ft/s.

Lau et al. (Ref 49) proposed a mathematical model predicting the particle behavior of nanocrystalline Ni powders during HVOF spray. They used a similar Lagrangian description of the particle interaction within the flame. The gas flow was modeled as ideal gas in a frictionless adiabatic duct. Their work indicated that fraction of the Ni-agglomerates did not melt during the HVOF process. Particles of 36 μm in size attain only 30% of the HVOF flame temperature during impact on the substrate. Particles with diameter of 15 μm reach a temperature of 1440 K during impact on the substrate. Eidelman and Yang (Ref 50) developed a three-dimensional model to simulate an HVOF process for nanoscale coating. They used traditional Favre averaged compressible Navier-Stokes equations with k-ε turbulence model for the continuum gas flow. Particle interaction with nozzle wall and the gas phase was formulated using a Lagrangian approach with key assumptions such as no temperature variation inside the particle, no intra-particle interaction and uniform particle properties. They observed that WC-Co particles of greater than 60 μm in size cannot be accelerated to greater than 33% of the maximum gas phase velocity and lead to porous coatings. Particles smaller than 10 μm were also found to decelerate in the stagnation zone and lead to very poor coating quality.

Basu and Cetegen (Ref 51) were the first to formulate a model for a new process of high-temperature coating, where liquid ceramic precursors can be injected into high-velocity oxy-flame to generate a high-quality dense oxide coating. The model incorporated the thermo physical phenomena that precursor droplets undergo when they are injected axially into the high-velocity flame. The processes within the droplet would be different from those during plasma spray as HVOF process is generally characterized by higher velocity and lower temperature as compared to DC-arc plasma. The modeling of HVOF jet was based on the consideration that the products from the combustion of stoichiometric mixture of oxy-propylene emerge out of the nozzle. The gaseous jet of HVOF was solved using k-ε turbulence model using the commercial FLUENT computational fluid dynamics code. The droplets injected into the flame underwent the processes of initial aerodynamic break-up, heating and surface evaporation with solute precipitation and internal vaporization and shell rupture. The precursor used for this study was zirconium acetate with mass fraction of 0.2. The aerodynamic break-up phenomenon was predicted using Taylor Aerodynamic Break-up (TAB) model. The model predicted that the axially injected (droplets are injected inside the HVOF flame jet) droplets were broken into smaller droplets of sizes ranging from 0.5 to 1 μm. However, in case of transverse injection (droplets are injected downstream) they experienced lower velocities and lesser amount of droplet break-up. Figure 27 (Ref 51) shows the droplet size distribution after aerodynamic break up in case of axial and transverse injection.

The second phase of the droplet processes considered vaporization and precipitation. These authors and others (Ref 36, 52, 53) reported that the evaporation process increases the solute concentration within the droplet in a plasma and HVOF jet. At some point, the solute concentration increases the supersaturation limit triggering precipitation. The model of Basu and Cetegen (Ref 51)

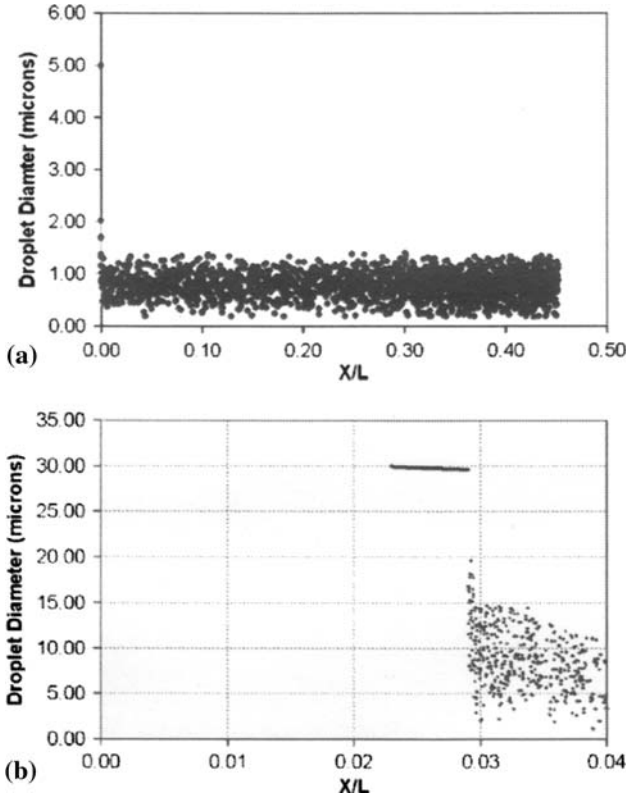

Fig. 27 Diameter distribution of (a) 5 μm axially injected and (b) 30 μm transversely injected droplets after shear break-up (Ref 51)

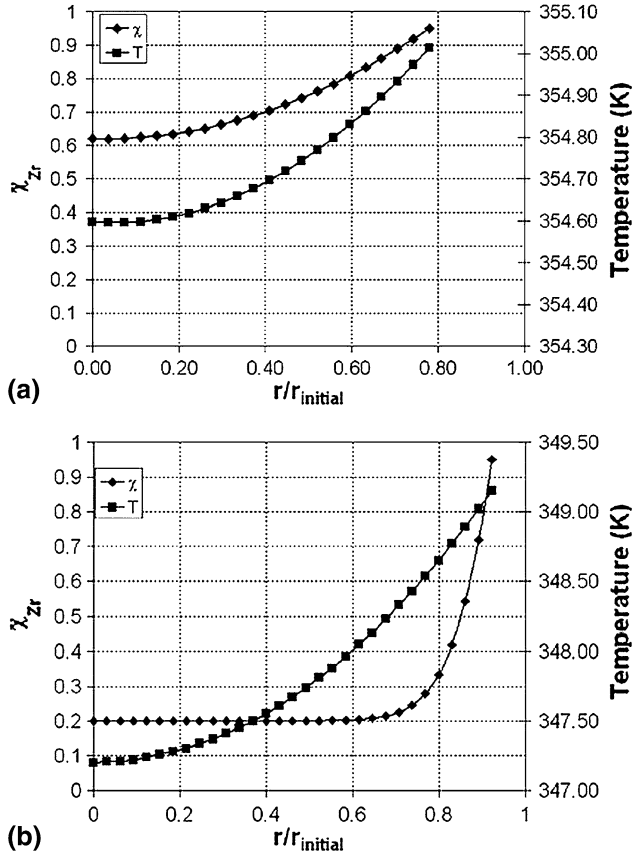

Fig. 28 Temperature and solute mass fraction profiles at the onset of precipitation for a droplet with initial size of (a) 5 μm and (b) 20 μm (Ref 51)

showed that the time involved in this precipitation process is longer than that in case of plasma injection. Figure 28 (Ref 51) shows the variation of solute mass and temperature within droplets whose initial diameters were 5 and 20 μm. It shows that the gradient of mass-fraction is greater than the gradient of temperature profile, indicating the higher thermal diffusivity than mass diffusivity. It also indicates that the smaller droplets tend to volumetrically precipitate while the larger droplets tend to form shell-type morphology.

A study of post-precipitation stage for the droplets of 10 and 20 μm was carried out by Basu and Cetegen for both plasma and HVOF (Ref 38, 51). The trapped liquid within the shell vaporizes to increase the internal pressure. The model showed that for both plasma and HVOF depending on the porosity of the formed shell, the internal pressure increases resulting in the rupture of the shell. This result also indicated that the time scale involved for this process is microseconds whereas the time scale for the precipitation process is of the order of milliseconds.

8. Multi-Scale Modeling of Thermal Spray Process

The studies described in previous sections portray only two important parts of the thermal spray processes, namely gas dynamics and particle/droplet transport processes. In order to describe the whole thermal spray process starting from gas dynamics to coating generation, a multi-scale modeling approach is necessary. There are few works in the literature that reported on modeling of the whole thermal spray process. In this section, some of these models are described briefly. The major work on multi-scale modeling of industrial HVOF thermal spray was carried out by Li et al. (Ref 30). In this work a Diamond Jet Hybrid HVOF thermal spray process for generating WC-12% Co coating was designed and modeled. Li et al. (Ref 30) focused on the multi-scale modeling and analysis of gas dynamics, in-flight behavior of particles and microstructure of generated coatings. Computational domain for this work includes both inside and outside of the nozzle. Eulerian approach was used in this model to solve the thermal and flow field of the gas phase, while the particle velocity, temperature and degree of melting were determined from a Lagrangian approach. Reynolds and Favre-averaged Navier-Stokes' equations were solved for modeling the gas dynamics. Nonequilibrium wall function treatment was used in renormalization group turbulence model to solve for the gas dynamics of flow at high Reynolds number with large pressure gradients within the nozzle. The eddy dissipation model was used for modeling

Table 2 Specified gas flow rate for parametric analysis of Diamond Jet hybrid HVOF gun (Ref 30)

Case	Propylene, scfh	Oxygen, scfh	Air, scfh	Nitrogen, scfh	$\dot{m}$, g/s	ϕ
1 (baseline)	176	578	857	28.5	18.10	1.045
2	176	578	428	28.5	13.73	1.186
3	176	867	857	28.5	21.35	0.756
4	264	867	1286	28.5	27.01	1.045

the chemistry. A first order upwind differencing scheme was used to solve for coupled mass, momentum and energy equation while second order upwind scheme was employed to capture the shock diamond that occurs in the external field. A fourth order Runge-Kutta method was used to solve for the velocity, temperature and melting degree of the particle. For predicting the microstructure of the coating, a stochastic approach was adopted. The powder particles were injected at the central inlet nozzle. N_2 was used as the particle carrier gas. The interaction between the hot combustion gases and particle results in momentum and energy transfer which leads to acceleration and heating of particles. Eventually, the particles in molten or semi-molten state exit the nozzle with a very high momentum and impact the cold and stationary substrate. The combustion process created an elevated temperature of 3000 K and the pressure of 6×10^5 Pa inside the combustion chamber. Table 2 compiles the conditions under which the parametric study was conducted by Li et al. (Ref 30).

In the simulation, the jet is over-expanded at the nozzle exit. For a small initial distance at the centerline, the concentration of N_2 carrier gas is higher but all the other species are almost absent. Due to rapid mixing and turbulence, the concentration of the carrier gas decreases and other species concentrations gradually increase within the nozzle. Outside the nozzle, due to entrainment of the static air, O_2 and N_2 contents increase rapidly. The very low mass fraction of propylene indicates a high degree of complete combustion inside the chamber. For the baseline condition in Table 2, the results show that the velocity and temperature profile also change with different spray distance. It can be noted that for each spray distance there is an optimum particle size for which the temperature is highest. It also shows that the velocity and temperature increase with increasing spray distance. The authors also reported that the effect of injection velocity is negligible on the impact velocity and temperature of the particle. Their analysis also showed that for industrial applications, the equivalence ratio should be around 1.2 for maximum mass flow rates.

Simulation of the coating microstructure was based on the energy conversion during the impact of the heated particles with the substrates, which dictates the temperature and degree of melting of the particles. The ideal condition of 100% melting of the particles would result in surface coating which is homogenous. However, when the presence of semi-molten or un-melted particles is taken into consideration, roughness and porosity increases in the microstructure. Figures 29 and 30 (Ref 30) suggest the presence of un-melted particles. For low melting ratio, the lower flow rates increase the porosity of the coating while for higher melting ratio, the lower flow rates reduce the porosity in the microstructure. Their results also predicted that very small sized particles are not effective for coating generation. The injection velocity did not have a significant effect on the coating and also the carrier gas flow rate must be kept to a minimum value to allow sufficient residence time for heat transfer between the particle and combustion gases. Similar such works were reported by Chandra et al. (Ref 54-56) for plasma and HVOF deposition. These models were also stochastic in nature and predicted the porosity, thickness and roughness of the coatings as a function of particle size, velocity, temperature, stand-off distance and injection methodology. To our knowledge, there has been no study performed on the multi-scale modeling of droplets in HVOF and plasma including stochastic analysis of the coating formation.

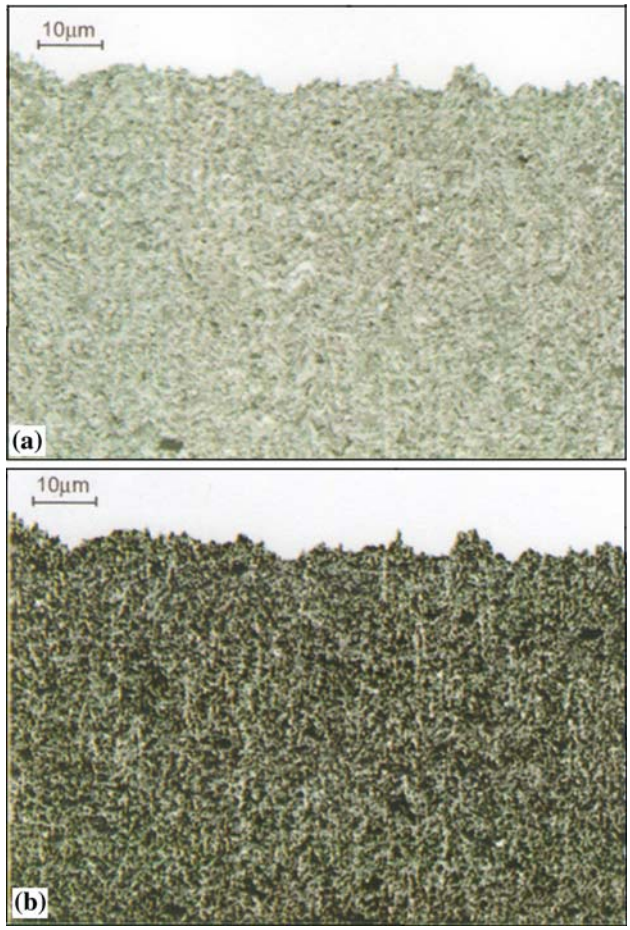

Fig. 29 Simulated (a) microstructure and (b) pore distribution in the coating made of particles of nonuniform molten states, which are deposited under baseline condition reported in Table 2 (Ref 30)

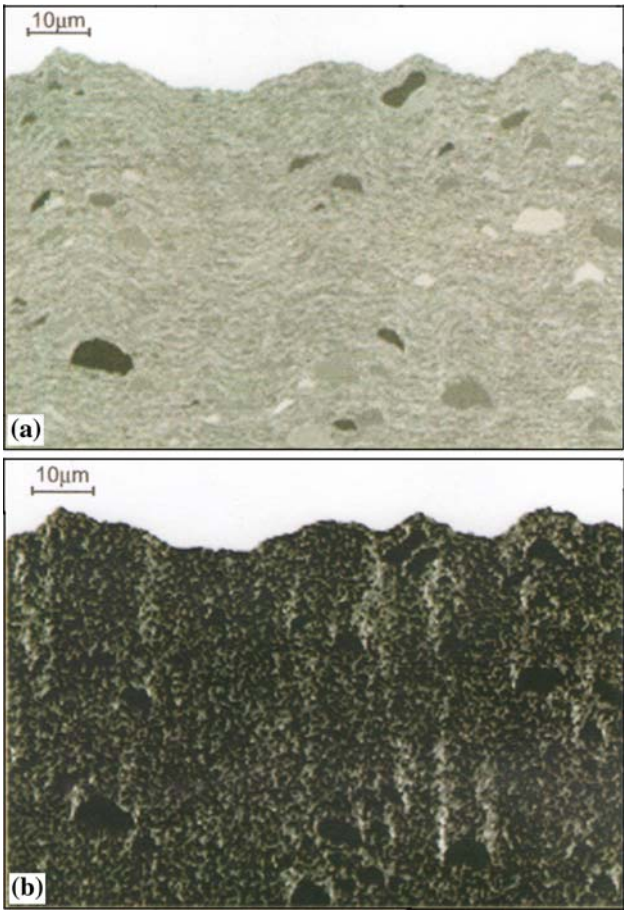

Fig. 30 Simulated (a) microstructure and (b) pore distribution in the coating made of particles of nonuniform molten states, which are deposited under condition in case 4 reported in Table 2 (Ref 30)

9. Conclusions and Recommendations

Thermal spray process has been typically modeled as three physically distinct segments: gas dynamics, gas-particle or gas-droplet interactions and coating deposition. Review of literature suggests that sophisticated models of both plasma and HVOF flame jets have been formulated. These models range from those that simulate the evolution of high-temperature jets with plasma or flame compositions to those that simulate the plasma and combustion process in detail. Powder or liquid spray injection into a plasma or a HVOF flame jet have been mostly modeled as the discrete phase of droplets and particles being heated in the computed thermal environment of a DC-arc plasma or HVOF flame jet. This type of treatment assumes that the discrete phase has very little or no effect on the flow and thermal fields of the plasma or HVOF flame jet, an assumption that is only valid for dilute particle or droplet regimes. In thermal spray applications where a larger amounts of powders or liquid precursors are to be processed, the dilute regime approximations will fail and the two-way coupling of the gas flow field with particles need to be taken into account. Eulerian-Lagrangian approach has been used to model the gas and particle interaction. The particle loading rate and the size distribution of the particles have a strong effect on the final temperature, velocity and melting ratio prior to impact on a substrate. Many authors have reported that most of the particles get deposited very near to the center of the jet. The coating develops when one molten particle gets deposited on another. The modeling the pattern of the coating is stochastic in nature, which involves statistical determination of splat size, coating thickness and porosity of the coating. It has been reported by many authors that size distribution, feeding-rate of particles and temperature of the flow fields have effects on the porosity and coating density.

In case of precursor droplets, the temperature and velocity of the gas fields also affect the internal liquid circulation and temperature distribution within droplets. Larger droplets usually undergo aerodynamic break-up. The droplets subsequently undergo fast vaporization and precipitation forming solid particles. The results show that the high velocity of HVOF jet facilitates the aerodynamic break up to higher degree, resulting in smaller droplets that are injected axially along the centerline of the high-temperature jet and can undergo faster vaporization and most likely generating splats of fully molten particles. However, for transverse injection, smaller droplets may not be properly entrained into the gas jet and hence can result in poor coating quality due to unpyrolized material arriving on the coating surface.

In the modeling of liquid precursor droplets being processed in a plasma or HVOF flame jet, one of the major knowledge gaps is the existence of comprehensive precipitation models that can be incorporated into heat and mass transfer models for liquid droplets of the type discussed in this article. For example, the current state-of-the-art in precipitation modeling of droplets in thermal sprays is limited to a homogeneous precipitation around precursor droplets that are based on studies at slow heating rates. The kinetics of solute precipitation experienced at rapid heating rates in plasmas and HVOF flame jets is an area that needs to be addressed in the future.

There are only few works available on the multi-scale modeling which involves end-to-end analysis of the thermal spray process. Modeling of the process that includes simulations of plasma or HVOF flame and at the same time calculate particle or droplet heat-up states in a coupled manner and also handle the deposition and coating formation would be desirable in the future. Such models can address the need for understanding multi-dimensional effects of each control parameter as well as determining the optimum conditions for particular coating microstructural requirement. With the advances in computational power and development of more sophisticated model components, the models of this type are envisaged to be important tools in the thermal spray field in the future. Finally, more detailed experimental results are needed to validate these models. With the advancement of optical diagnostic techniques, it is anticipated that more detailed experimental results will be available in the future.

Acknowledgments

The authors acknowledge the past financial support by the Office of Naval Research under the direction of Dr. Larry Kabacoff. Many useful discussions took place during the course of our modeling studies with our colleagues Professors Maury Gell, Nitin Padture and Eric Jordan. We are also grateful to Kaushik Saha and Abhishek Saha for their help in the literature search.

References

1. K. Masters, *Spray Drying Handbook*, 4th ed., Wiley, New York, 1985
2. L. Pawlowski, *The Science and Engineering of Thermal Spray Coatings*, Wiley, Chichester, 1995
3. N.P. Padture, K.W. Schlichting, T. Bhatia, A. Ozturk, B.M. Cetegen, E.H. Jordan, and M. Gell, Towards Durable Thermal Barrier Coatings with Novel Microstructures Deposited by Solution-Precursor Plasma Spray, *Acta Mater.*, 2001, **49**, p 2251-2257
4. E.H. Jordan, L. Xie, X. Ma, M. Gell, N.P. Padture, B.M. Cetegen, A. Ozturk, J. Roth, T.D. Xiao, and P.E. Bryant, Superior Thermal Barrier Coatings Using Solution Precursor Plasma Spray, *J. Therm. Spray Technol.*, 2004, **13**(1), p 57-65
5. T. Bhatia, A. Ozturk, L. Xie, E. Jordan, B.M. Cetegen, M. Gell, X. Ma, and N. Padture, Mechanisms of Ceramic Coating Deposition in Solution-Precursor Plasma Spray, *J. Mater. Res.*, 2002, **17**(9), p 2363-2372
6. N. Padture, M. Gell, and E.H. Jordan, Thermal Barrier Coatings for Gas Turbine Engine Applications, *Science*, 2002, **296**, p 280-284
7. M.I. Boulos, P. Fauchais, and E. Pfender, *Thermal Plasmas: Fundamentals and Applications*, Springer
8. J.D. Ramshaw and C.H. Chang, Computational Fluid Dynamics Modeling of Multicomponent Thermal Plasmas, *Plasma Chem. Plasma Process.*, 1992, **12**(3), p 299-325
9. C.H. Chang and J.D. Ramshaw, Numerical Simulation of Non-equilibrium Effects in an Argon Plasma Jet, *Phys. Plasmas*, 1994, **1**(11), p 3698-3708
10. A.H. Dilawari, J. Szekely, and R. Westhoff, A Comparison of Experimental Measurements and Theoretical Predictions Regarding the Behavior of a Turbulent Argon Plasma Jet Discharging into Air, *Plasma Chem. Plasma Process.*, 1990, **10**, p 321
11. J.P. Trelles, E. Pfender, and J.V.R. Heberlein, Modelling of the Arc Reattachment Process in Plasma Torches, *J. Phys. D*, 2007, **40**, p 5635-5648
12. J.P. Trelles, J.V.R. Heberlein, and E. Pfender, Non-equilibrium Modelling of Arc Plasma Torches, *J. Phys. D*, 2007, **40**, p 5937-5952
13. J.P. Trelles, E. Pfender, and J.V.R. Heberlein, Thermal Non-equilibrium Simulation of an Arc Plasma Jet, *IEEE Trans. Plasma Sci.*, 2008, **36**(4), p 1026-1027
14. C. Marchand, A. Vardelle, G. Mariaux, and P. Lefort, Modelling of the Plasma Spray Process with Liquid Feedstock Injection, *Surf. Coat. Technol.*, 2008, **202**, p 4458-4464
15. A. Vardelle, C. Chazelas, C. Marchand, and G. Mariaux, Modeling Time-dependent Phenomena in Plasma Spraying of Liquid Precursors, *Pure Appl. Chem.*, 2008, **80**(9), p 1981-1991
16. H.P. Li and X. Chen, Three-Dimensional Modeling of the Turbulent Plasma Jet Impinging upon a Flat Plate and with Transverse Particle and Carrier-Gas Injection, *Plasma Chem. Plasma Process.*, 2002, **22**(1), p 27-58
17. X. Chen and E. Pfender, Behavior of Small Particles in a Thermal Plasma Flow, *Plasma Chem. Plasma Process.*, 1983, **3**(3), p 351-366
18. Y.C. Lee, Y.P. Chyou, and E. Pfender, Particle Dynamics and Particle Heat and Mass Transfer in Thermal Plasmas. Part II. Particle Heat and Mass Transfer in Thermal Plasmas, *Plasma Chem. Plasma Process.*, 1985, **5**(4), p 391-414
19. X. Chen and E. Pfender, Effect of the Knudsen Number on Heat Transfer to a Particle Immersed into a Thermal Plasma, *Plasma Chem. Plasma Process.*, 1983, **3**(1), p 97-113
20. Y.C. Lee and E. Pfender, Particle Dynamics and Particle Heat and Mass Transfer in Thermal Plasmas. Part III. Thermal Plasma Jet Reactors and Multiparticle Injection, *Plasma Chem. Plasma Process.*, 1987, **7**(1), p 1-27
21. H.B. Xiong, L.L. Zheng, S. Sampath, R.L. Williamson, and J.R. Fincke, Three-Dimensional Simulation of Plasma Spray: Effects of Carrier Gas Flow and Particle Injection on Plasma Jet and Entrained Particle Behavior, *Int. J. Heat Mass Transf.*, 2004, **47**, p 5189
22. R.M. Young and E. Pfender, Generation and Behavior of Fine Particles in Thermal Plasmas—A Review, *Plasma Chem. Plasma Process.*, 1985, **5**(1), p 1-36
23. X. Chen, Plasma Particle Momentum Transfer under Conditions of Great Knudsen Numbers and Thin Plasma Sheath, *Plasma Chem. Plasma Process.*, 1996, **16**(1), p 71S-82S
24. X. Chen and E. Pfender, Unsteady Heating and Radiation Effects of Small Particles in a Thermal Plasma, *Plasma Chem. Plasma Process.*, 1982, **2**(3), p 293-316
25. F.B. Ettouil, B. Pateyron, H. Ageorges, M. El Ganaoui, P. Fauchais, and O. Mazhorova, Fast Modeling of Phase Changes in a Particle Injected within a D.C. Plasma Jet, *J. Therm. Spray Technol.*, 2007, **16**(5-6), p 744-750
26. T.A. Dobbins, R. Knight, and M.J. Mayo, HVOF Thermal Spray Deposited Y_2O_3-Stabilized ZrO_2 Coatings for Thermal Barrier Applications, *J. Therm. Spray Technol.*, 2003, **12**(2), p 214-225
27. C.H. Lee and K.O. Min, Effects of Heat Treatment on the Microstructure and Properties of HVOF-Sprayed Ni–Cr–W–Mo–B Alloy Coatings, *Surf. Coat. Technol.*, 2000, **132**(1), p 49-57
28. D.A. Stewart, P.H. Shipway, and D.G. McCartney, Abrasive Wear Behaviour of Conventional and Nanocomposite HVOF-Sprayed WC–Co Coatings, *J. Wear*, 1999, **225-229**(Part 2), p 789-798
29. M. Li and P.D. Christofides, Computational Study of Particle In-Flight Behavior in the HVOF Thermal Spray Process, *Chem. Eng. Sci.*, 2006, **61**(19), p 6540-6552
30. M. Li and P.D. Christofides, Multi-Scale Modeling and Analysis of an Industrial HVOF Thermal Spray Process, *Chem. Eng. Sci.*, 2005, **60**(13), p 3649-3669
31. M. Li, D. Shi, and P.D. Christofides, Modeling and Control of HVOF Thermal Spray Processing of WC–Co Coatings, *Powder Technol.*, 2005, **156**, p 177-194
32. S. Gu, C.N. Eastwick, K.A. Simmons, and D.G. McCartney, Computational Fluid Dynamic Modeling of Gas Flow Characteristics in a High-Velocity Oxy-Fuel Thermal Spray System, *J. Therm. Spray Technol.*, 2001, **10**(3), p 461-469
33. B. Hassan, A.R. Lopez, and W.L. Oberkampf, Computational Analysis of a Three-Dimensional High-Velocity Oxygen Fuel (HVOF) Thermal Spray Torch, *J. Therm. Spray Technol.*, 1998, **7**(1), p 71-77
34. G.V. Jayanthi, S.C. Zhang, and G.L. Messing, Modeling of Solid Particle Formation During Solution Aerosol Thermolysis, *Aerosol Sci. Technol.*, 1993, **19**, p 478-490
35. G.L. Messing, S.C. Zhang, and G.V. Jayanthi, Ceramic Powder Synthesis by Spray Pyrolysis, *J. Am. Ceram. Soc.*, 1993, **76**, p 2707-2726
36. A. Ozturk and B.M. Cetegen, Modeling of Axially and Transversely Injected Precursor Droplets into a Plasma Environment, *Int. J. Heat Mass Transf.*, 2005, **48**, p 4367-4383
37. W.A. Sirignano, *Fluid Dynamics and Transport of Droplets and Sprays*, Cambridge University Press, Cambridge, 1999
38. S. Basu and B. Cetgen, Modeling of Thermo-physical Processes in Liquid Ceramic Precursor Droplets Injected into a Plasma Jet, *Int. J. Heat Mass Transf.*, 2007, **50**(17-18), p 3278
39. S. Basu, E.H. Jordan, and B.M. Cetegen, Fluid Mechanics and Heat Transfer of Liquid Precursor Droplets Injected into High-Temperature Plasmas, *J. Therm. Spray Eng.*, 2008, **17**
40. S.-C. Zhang, G.L. Messing, and M. Borden, Synthesis of Solid, Spherical Zirconia Particles by Spray Pyrolysis, *J. Am. Ceram. Soc.*, 1990, **73**(1), p 61-67

41. S. Jain, D.J. Skamser, and T.T. Kodas, Morphology of Single-Component Particles Produced by Spray Pyrolysis, *Aerosol Sci. Technol.*, 1997, **27**, p 575-590
42. S. Che, O. Sakurai, K. Shinozaki, and N. Mizutani, Particle Structure Control Through Intraparticle Reactions by Spray Pyrolysis, *J. Aerosol Sci.*, 1998, **29**(3), p 271-278
43. W. Nimmo, D. Hind, H.J. Ali, E. Hampartsoumian, and S.J. Milne, The Production of Ultrafine Zirconium Oxide Powders by Spray Pyrolysis, *J. Mater. Sci.*, 2002, **37**, p 3381-3387
44. J.-C. Lin and J.W. Gentry, Spray Drying Drop Morphology: Experimental Study, *Aerosol Sci. Technol.*, 2003, **37**, p 15-32
45. W. Yu, ''Diagnostics of the Particle Field in Particle-laden DC-ARC plasmas and High Velocity Combustion Jets as Applied to Industrial Thermal Sprays,'' Ph.D. Thesis, University of Connecticut, 1999
46. C. Bartuli, T. Valente, F. Cipri, E. Bemporad, and M. Tului, Parametric Study of an HVOF Process for the Deposition of Nanostructured WC-Co Coatings, *J. Therm. Spray Technol.*, 2005, **14**(2), p 187-195
47. E. Dongmo, M. Wenzelburger, and R. Gadow, Analysis and Optimization of the HVOF Process by Combined Experimental and Numerical Approaches, *J. Surf. Coat. Technol.*, 2008, **202**(18), p 4470-4478
48. H.H. Tawfik and F. Zimmerman, Mathematical Modeling of the Gas and Powder Flow in HVOF Systems, *J. Therm. Spray Technol.*, 1997, **6**, p 345
49. M.L. Lau, V.V. Gupta, and E.J. Lavernia, Mathematical Modeling of Particle Behavior of Nanocrystalline Ni During High Velocity Oxy-Fuel Thermal Spray in Nanostructured Materials, *Nanostruct. Mater.*, 1998, **10**(5), p 715
50. S. Eidelman and X. Yang, Three Dimensional Simulation of HVOF Spray Deposition of Nanoscale Materials, *Nanostruct. Mater.*, 1997, **9**(1-8), p 79-84
51. S. Basu and B.M. Cetegen, Modeling of Liquid Ceramic Precursor Droplets in a High Velocity Oxy-Fuel Flame Jet, *Acta Mater.*, 2008, **56**(12), p 2750-2759
52. A. Ozturk and B.M. Cetegen, Modeling of Precipitate Formation in Precursor Droplets Injected Axially into an Oxygen/Acetylene Combustion Flame, *Mater. Sci. Eng.: A*, 2006, 422(1-2), p 163-175
53. A. Ozturk and B.M. Cetegen, Morphology of Ceramic Particulates Formed in a Premixed Oxygen/Acetylene Flame from Mono-Size Liquid Precursor Droplets, *Acta Mater.*, 2005, **53**, p 2531-2544
54. R. Ghafouri-Azar, J. Mostaghimi, S. Chandra, and M. Charmchi, A Stochastic Model to Simulate the Formation of a Thermal Spray Coating, *J. Therm. Spray Technol.*, 2003, **12**, p 53-69
55. M. Pasandideh-Fard, S. Chandra, and J. Mostaghimi, A Three-Dimensional Model of Droplet Impact and Solidification, *Int. J. Heat Mass Transf.*, 2002, **45**, p 2229-2242
56. J. Mostaghimi, S. Chandra, R. Ghafouri-Azar, and A. Dolatabadi, Modeling Thermal Spray Coating Processes: A Powerful Tool in Design and Optimization, *Surf. Coat. Technol.*, 2003, **163-164**, p 1-11